Magneto-Optical effects in metamaterials for the design of opto-mechanical devices

Jaime Andrés Girón Sedas

Thesis submitted as a partial requirement for the degree of Doctor in Physics

Advisors: Juan Carlos Granada Echeverry
Jorge Ricardo Mejía Salazar

UNIVERSIDAD DEL VALLE
FACULTAD DE CIENCIAS NATURALES Y EXACTAS
POSGRADO EN CIENCIAS FÍSICA
SANTIAGO DE CALI

2018

Certificate of thesis approval

Universidad del Valle

FACULTAD DE CIENCIAS NATURALES Y EXACTAS
ACTA DE SUSTENTACIÓN
TESIS DE DOCTORADO EN CIENCIAS-FÍSICA

Estudiante:	**JAIME ANDRÉS GIRÓN SEDAS**
Código:	1504722
Título de la Tesis:	**"MAGNETO-OPTICAL EFFECTS IN METAMATERIALS FOR THE DESIGN OF OPTO-MECHANICAL DEVICES"**
Fecha y Hora:	jueves 26 de abril de 2018, a las 10:00 a.m.
Directores:	Dr. Juan Carlos Granada Echeverry. Dr. Jorge Ricardo Mejía Salazar.
Jurados:	Dr. Francisco Rodríguez Fortuño, King's College London, Inglaterra. Dr. Ernesto Reyes Gómez, Universidad de Antioquia, Medellín. Dr. Guillermo Javier Madroñero Pabón, Departamento de Física, Universidad del Valle.

RESULTADO DE LA EVALUACIÓN

( ) APROBADA ( ) MERITORIA (X) LAUREADA

Si la nota es Meritoria o Laureada, el jurado deberá sustentarla en hoja separada con la firma de todos ellos y anexarla al Acta.

( ) REPROBADA El estudiante debe matricularse nuevamente en esta actividad.

( ) PENDIENTE El estudiante debe acoger las recomendaciones del jurado y presentar nuevamente el documento ante el Director de Tesis. Requiere ( ) / No requiere ( ) nueva sustentación.

El plazo para nueva sustentación y/o presentación del documento final es de ____________________.

OBSERVACIONES:

El jurado recomienda Tesis Laureada

.

Santiago de Cali, 26 de abril de 2018.

Dr. Francisco Rodríguez Fortuño
Jurado

Dr. Ernesto Reyes Gómez
Jurado

Dr. Javier Madroñero Pabón
Jurado

Juan Carlos Granada E.

Dr. Juan Carlos Granada Echeverry
Director de Tesis

Ricardo Mejía

Dr. Jorge Ricardo Mejía Salazar
Director de Tesis

Dr. Eval Baca Miranda
Coordinador de la sustentación
Director de programa

Abstract

In this thesis, we demonstrated two different mechanisms for the enhancement of the transverse magneto-optical Kerr effect (TMOKE). In the first one, we show extraordinary values of the TMOKE for the resonant tunneling modes in trilayer structures, featuring a dielectric slab sandwiched between two magneto-optical metallic layers. In the second case, we used the new and unusual physical properties of the epsilon-near-zero (ENZ) metamaterials to enhance the TMOKE up to giant values, through the coupling of perfect absorbing and surface plasmon-polariton modes, in a multilayer magneto-plasmonic structure. Potential applications in the development of unprecedented miniaturizable plasmonic biosensing platforms are shown. On the other hand, the control of optical forces on polarized particles emitting near a magneto-optical surface is demonstrated, thus opening new routes for the manipulation of nanoparticles. All numerical results were obtained by using the generalized scattering-matrix approach for magneto-optics in periodically patterned multilayer systems. In the calculations of optical forces, we used the scattering-matrix method combined with the formalism of Green's functions to obtain the corresponding numerical data.

Resumen

En esta tesis, demostramos dos mecanismos diferentes para la mejora del efecto de Kerr transversal magneto-óptico (TMOKE). En el primero, mostramos valores extraordinarios del TMOKE mediante la exitación de modos de tunelamiento resonante en una tri-capa, con una capa dieléctrica intercalada entre dos capas metálicas magnetoópticas. En el segundo caso, utilizamos las nuevas propiedades físicas e inusuales de los metamateriales épsilon-near-zero (ENZ) para mejorar el TMOKE hasta valores gigantes, a través del acoplamiento de modos de absorción perfecta y plasmones de superficie, en una estructura magneto-plasmónica. Se muestran aplicaciones potenciales en el desarrollo de plataformas de biosensores plasmónicos miniaturizables sin precedentes. Por otro lado, se muestra una nueva forma de controlar las fuerzas ópticas sobre partículas polarizadas cerca de superficies magnetoópticas, abriendo así nuevas rutas para la manipulación de nanopartículas. Todos los resultados numéricos se obtuvieron utilizando el enfoque de matriz de dispersión generalizada para magnetoóptica en sistemas multicapa de diseño periódico. En los cálculos de fuerzas ópticas, utilizamos el método de matriz de dispersión combinado con el formalismo de las funciones de Green para obtener los datos numéricos correspondientes.

Publications from this work

- J. A. Girón-Sedas, J. R. Mejía-Salazar, E. Moncada-Villa and N. Porras-Montenegro, *Appl. Phys. Lett.* **109**, 033106 (2016).

- J. A. Girón-Sedas, J. R. Mejía-Salazar, J. C. Granada, and Osvaldo N. Oliveira Jr., *Phys. Rev. B* **94**, 245230 (2016).

- J. A. Girón-Sedas, F. Réyes Gómez, Pablo Albella, J. R. Mejía-Salazar and Osvaldo N. Oliveira Jr., *Phys. Rev. B* **96**, 075415 (2017).

Acronyms

ENZ Epsilon-Near-Zero

HED Horizontal Electric Dipole

MO Magneto-Optical

NF Near Field

SPP Surface Plasmon Polariton

SPR Surface Plasmon-Resonances

TMOKE Transverse Magneto-Optical Kerr Effect

VED Vertical Electric Dipole

List of Figures

Contents

Chapter 1

Introduction

The first magneto-optical (MO) effect was observed in 1846 when Michael Faraday found a rotation of the polarization plane of a linearly polarized light transmitted through a gyrotropic slab placed in a static magnetic field, as depicted in Fig. (1.1). This phenomenon is commonly known as Faraday effect[1]. On the other hand, in 1877, the reverend Jhon Kerr reported weaker rotations of the plane of polarization when a linearly polarized electromagnetic wave is reflected on the interface between air and a magnetized slab. This last effect, also illustrated in Fig.(1.1), is known as the MO polar Kerr rotation[2]. Both magneto-optical effects arise as a result of the interaction between light and a medium that has been altered by the presence of a magnetic field, exhibiting an ellipticity change of the electromagnetic wave.

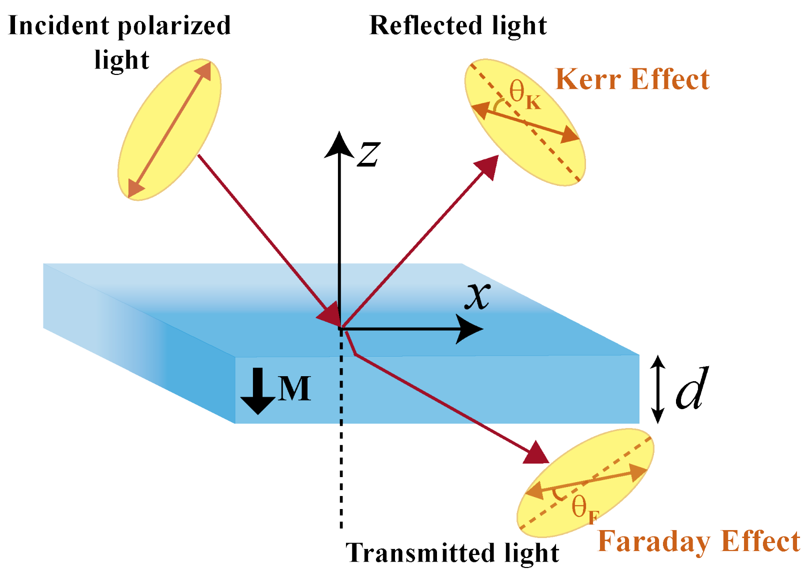

Figure 1.1: Schematic representation of the Faraday and Kerr effect in a slab of thickness d with a spontaneous magnetization $\mathbf{M}$. The rotation of the polarization planes of the transmitted and reflected light are characterized by the angles θ_F and θ_K, respectively.

In particular, the MO Kerr effects can be classified according to the relative orientation of the wavevector $\mathbf{k}$ of the incident electromagnetic wave respect to the magnetic field or magnetization $\mathbf{M}$, see details in Fig. 1.2. In the polar and the longitudinal geometries, the wavevector of the electromagnetic wave has a component along the magnetization of the sample. In such cases, the components of the electromagnetic field are coupled by the non-diagonal elements of the dielectric permittivity tensor, producing a rotation of the polarization plane. In the transversal geometry, the incidence plane is perpendicular to the magnetization (magnetic field) in the sample, $\mathbf{M}$. In this case, only the p-polarized incident light is affected by the applied magnetic field. This means that the polarization plane does not suffer any change, while there is a change in the reflected intensity for such polarization. This MO effect is known as transversal MO Kerr effect (TMOKE) and is defined as

$$\text{TMOKE} = \frac{R_{\text{pp}}\,(+\mathbf{M}) - R_{\text{pp}}\,(-\mathbf{M})}{R_{\text{pp}}\,(+\mathbf{M}) + R_{\text{pp}}\,(-\mathbf{M})}, \tag{1.1}$$

where the signs $+$ and $-$ denote the sense of $\mathbf{M}$ along the corresponding axis.

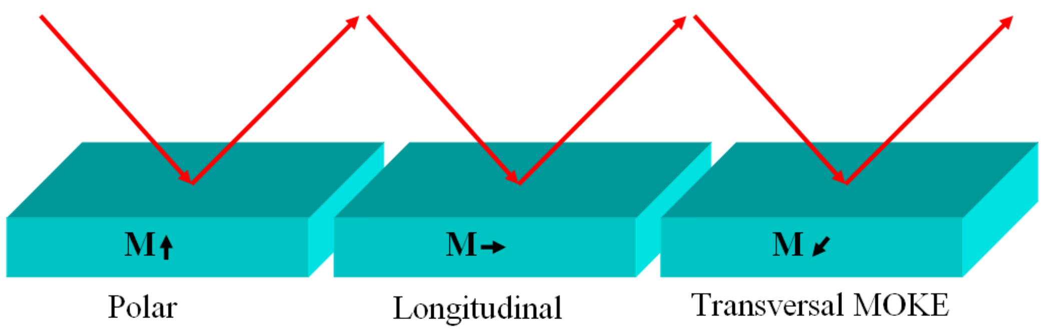

Figure 1.2: The three possible MO configurations, defined regarding the relative orientation between the magnetic field and the plane of incidence.

The investigation of these mentioned effects has been a subject of great interest during the last decades due to their potential applications in the design and development of magnetic-storage, biosensing, and optical isolation devices.[3–6] Some recent achievements have shown the possibility for ultrafast control of a medium magnetization at the subpicosecond time scale via light,[7–9] which is of prime importance for modern magnetic storage systems demanding very large operation rates. The main concept behind these achievements is the manipulation and control of the Kerr and Faraday magneto-optical effects.[10–17] In particular, the transverse magneto-optical Kerr effect (TMOKE), useful for magnetization monitoring in different types of magnetic samples,[3,4] is the basis of some biosensing[5] and optical filtering devices,[6] and some data storage devices use it to read the data from magnetic disks.[18,19] In the case of conventional ferromagnetic materials[20] the TMOKE has values as small as 10^{-3}, which limits its applicability. Thus, it is desirable to find new ways to enhance it. The most works in this direction have been mainly focused on the resonant excitation of surface plasmon polaritons (SPP), because this resonant excitation brings as consequence an enhanced electromagnetic field in the interior of the MO layers.[10–15] This stimulated a new area of research called Magneto-Plasmonic,[21] i.e., a mixture of magnetic and plasmonic properties. Most recent studies have employed a hybrid excitation of waveguide-plasmon polariton modes.[15] However, there are some drawbacks, which emerge when we need to excite SPPs: 1) the conventional Kretschmann geometry shows rather difficulty because the refractive index of the prism must be larger than the refractive index of the dielectric background.[22] 2) The need to use a prism for the excitation of SPPs, which impairs the miniaturization process and development of modern devices. Although grating coupler platforms allow for miniaturization, we should note that surface plasmon resonance excitation depends on the diffraction order, ridge geometry, and the period length of the system, which requires a complex design. Recently, the excitation of SPPs without a prism or grating coupler has been achieved experimentally [23] by controlling light absorption in nanostructured indium tin oxide (ITO) films operating in the ε-near-zero (ENZ) frequency regime.[24–26] All the previous works have used complex structures to excite surface plasmon polaritons and improving the TMOKE. However, these systems show some problems in the process of miniaturization, affecting directly in the development of modern devices. In this respect, we have made two unprecedented theoretical contributions, addressing the mentioned issues and guaranteeing giant values of TMOKE with very simple systems[27,28]. The first one is via resonant tunneling modes in a trilayer structure, while the second one uses the direct coupling of surface plasmon polaritons in MO epsilon-near-zero structures. Moreover, we showed for first time a realistic structure with giant values of TMOKE, which can be used in the design of biosensors. These new devices could have potential aplications for early detection of some diseases or probing levels of air pollution, which are timely for reducing the mortality rates around the world.

On the other hand, the repulsion of particles from surfaces through an action at a distance is relevant for technological applications where adhesion[29] and stiction[30] at the nanoscale need to be reduced. Such unwanted effects occur mainly because capillary, electrostatic and van der Waals forces dominate over the elastic restoring forces during fabrication or functioning.[29–31] This repulsion has been reached using radiation pressure[32,33] and Casimir-Lifshitz forces,[34–36] which require an external agent for inducing the repulsive force. In this context, isotropic[37] or anisotropic[38] epsilon-near-zero (ENZ) metamaterials are promising because no external agent is necessary for establishing the repulsive force. These ENZ-metamaterials can be implemented with natural materials near their plasma frequencies or by means of artificial metamaterials, but they possess several limitations. For example, around the resonant plasma frequency absorption reaches high values,[37] and experimentally available artificial ENZ metamaterials are only functional for a specific polarization of light.[38–40] Here, we show, for the first time, that MO-metamaterials may have advantages in generating the repulsive force without the above mentioned limitations. In particular, we have employed an architecture for MO-metamaterials,[41] *i.e.*, artificial materials with a strongly enhanced MO response, for which repulsive forces act on polarized particles under the condition of transversal magnetization. The conditions required for the repulsive force were determined by analytical calculations within the near-field (NF) approximation. In contrast to previous proposals,[37–46] we have shown that it is possible to obtain repulsive forces in a broad range at the optical regime, which may work even far from the ENZ condition. This constitutes a great advantage for the design of new devices for the control of nanoparticles.

This thesis is organized as follows. A general introduction is given in Chapter 1. In Chapter 2 we present the theoretical framework. The Chapter 3 shows a brief description of the magneto-optical Kerr configurations, focusing in the TMOKE and some ways to enhance it. In the Chapter 4 we analyze the repulsion of polarized particles near a surface. Finally, the conclusions are presented in section 5.

Chapter 2

Approaches for the study of electromagnetic waves propagation in anisotropic multilayers system

Contents

There are several techniques for the study of propagation of electromagnetic waves in multilayer anisotropic systems. In this work, we used the scattering matrix method.[48,49] The basic ideas behind this method is briefly described in section 2.1.

2.1 Scattering matrix

Although the transfer matrix method discussed in the previous section constitutes a powerful skill for the study of the electrodynamical properties of the considered systems, in many contexts it is desirable to use the scattering matrix formalism. In this section we briefly describe this approach, which we have employed for the analysis of propagation of electromagnetic waves our anisotropic multilayer system[48,49]. The optical properties of each layer are described by a homogeneous dielectric tensor $\bar{\bar{\varepsilon}}$, and the electromagnetic fields are assumed in the form

$$\mathbf{E}(\mathbf{r}, z) = e^{i\mathbf{k}\cdot\mathbf{r}} e^{iqz} \left[e_x \hat{\boldsymbol{x}} + e_y \hat{\boldsymbol{y}} + e_z \hat{\boldsymbol{z}}\right] = e^{i\mathbf{k}\cdot\mathbf{r}} e^{iqz} \boldsymbol{e}, \tag{2.1}$$

$$\mathbf{H}(\mathbf{r}, z) = e^{i\mathbf{k}\cdot\mathbf{r}} e^{iqz} \left[h_x \hat{\boldsymbol{x}} + h_y \hat{\boldsymbol{y}} + h_z \hat{\boldsymbol{z}}\right] = e^{i\mathbf{k}\cdot\mathbf{r}} e^{iqz} \boldsymbol{h}, \tag{2.2}$$

where $\mathbf{k} = (k_x, k_y)$ is wave vector parallel to the interfaces and q stands for the z-component of the wave vector. With this choice, the Maxwell's equations are converted into the following non-linear eigenvalue problem for the magnetic field[48,49]

$$\left(\mathcal{A}_2 q^2 + \mathcal{A}_1 q + \mathcal{A}_0 + \mathcal{A}_{-1}\frac{1}{q}\right)\begin{pmatrix} h_x \\ h_y \end{pmatrix} = 0, \tag{2.3}$$

where the 2×2 matrices $\mathcal{A}_i$ are given by

$$
\begin{aligned}
\mathcal{A}_2 &= \begin{pmatrix} \eta_{yy} & -\eta_{yx} \\ -\eta_{xy} & \eta_{xx} \end{pmatrix}, \\
\mathcal{A}_1 &= \mathcal{A}_1^{(a)} + \mathcal{A}_1^{(b)} = \begin{pmatrix} -k_y\eta_{zy} & k_y\eta_{zx} \\ k_x\eta_{zy} & -k_x\eta_{zx} \end{pmatrix} + \begin{pmatrix} -k_y\eta_{yz} & k_x\eta_{yz} \\ k_y\eta_{xz} & -k_x\eta_{xz} \end{pmatrix}, \\
\mathcal{A}_0 &= \mathcal{A}_0^{(a)} + \mathcal{A}_0^{(b)} - \frac{\omega^2}{c^2}\hat{1} = \eta_{zz}\begin{pmatrix} k_y^2 & -k_yk_x \\ -k_xk_y & k_x^2 \end{pmatrix} \\
&+ \begin{pmatrix} \eta_{yy}k_x^2 - \eta_{yx}k_yk_x & \eta_{yy}k_xk_y - \eta_{yx}k_y^2 \\ \eta_{xx}k_yk_x - \eta_{xy}k_x^2 & \eta_{xx}k_y^2 - \eta_{xy}k_xk_y \end{pmatrix} - \frac{\omega^2}{c^2}\hat{1}, \\
\mathcal{A}_{-1} &= \begin{pmatrix} \eta_{zx}k_y^2k_x - \eta_{zy}k_yk_x^2 & \eta_{zx}k_y^3 - \eta_{zy}k_y^2k_x \\ \eta_{zy}k_x^3 - \eta_{zx}k_x^2k_y & \eta_{zy}k_x^2k_y - \eta_{zx}k_xk_y^2 \end{pmatrix}.
\end{aligned}
\tag{2.4}
$$

This non-linear eigenvalue problem may be reformulated as a generalized linear eigenvalue problem[49], whose numerical solution is achieved in a relatively easy way with the use of standard routines of linear algebra (**LAPACK**[1]).

Electromagnetic fields

The solution of the eigenvalue problem Eq. (2.3) gives four non vanishing eigenvalues, two of them, denoted as q_n (p_n), with positive (negative) imaginary part and corresponding to the eigenvector $\phi_n = (\phi_{x_n}, \phi_{y_n})^T$ $[\varphi_n = (\varphi_{x_n}, \varphi_{y_n})^T]$. We are interested in the field components $\boldsymbol{e}_{||} = (-e_y, e_x)^T$ and $\boldsymbol{h}_{||} = (h_x, h_y)^T$, which are continuous at the different interfaces in the multilayer. It is straightforward to show that in the lth layer these field components are written as

$$
\begin{pmatrix} \boldsymbol{e}_{||}(z) \\ \boldsymbol{h}_{||}(z) \end{pmatrix}_l = \begin{pmatrix} \hat{M}_{11} & \hat{M}_{12} \\ \hat{M}_{21} & \hat{M}_{22} \end{pmatrix}_l \begin{pmatrix} \hat{f}_l^{+}(z)\boldsymbol{a}_l \\ \hat{f}_l^{-}(d_l - z)\boldsymbol{b}_l \end{pmatrix} = \hat{M}_l \begin{pmatrix} \hat{f}_l^{+}(z)\boldsymbol{a}_l \\ \hat{f}_l^{-}(d_l - z)\boldsymbol{b}_l \end{pmatrix}, \tag{2.5}
$$

where $\boldsymbol{a}_l = (a_{l,1}, a_{l,2})^T$ and $\boldsymbol{b}_l = (b_{l,1}, b_{l,2})^T$ are the forward and backward amplitudes, respectively, and $\hat{f}_+(z) = \mathrm{diag}\left\{e^{iq_1z}, e^{iq_2z}\right\}$ and $\hat{f}_-(z) = \mathrm{diag}\left\{e^{-ip_1z}, e^{-ip_2z}\right\}$. The elements of layer matrix $\hat{M}$ are defined as

$$
\begin{aligned}
\hat{M}_{11} &= \left[\mathcal{A}_0^{(b)}\Phi_+\hat{q}^{-1} + \mathcal{A}_1^{(b)}\Phi_+ + \mathcal{A}_2\Phi_+\hat{q}\right], \\
\hat{M}_{12} &= \left[\mathcal{A}_0^{(b)}\Phi_-\hat{p}^{-1} + \mathcal{A}_1^{(b)}\Phi_- + \mathcal{A}_2\Phi_-\hat{p}\right], \\
\hat{M}_{21} &= \Phi_+, \\
\hat{M}_{22} &= \Phi_-,
\end{aligned}
\tag{2.6}
$$

[1] **LAPACK** documentation is available at http://www.netlib.org/lapack.

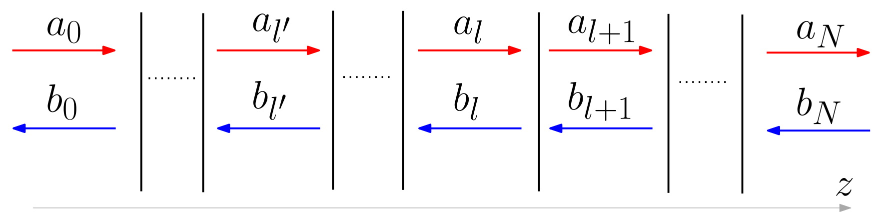

Figure 2.1: Schematic representation of the forward and backward amplitudes in a multilayer structure. Notice that the boundary between successive layers is parallel to the xy plane.

with $\hat{q} = \mathrm{diag}\,\{q_1, q_2\}$ and $\hat{p} = \mathrm{diag}\,\{p_1, p_2\}$. Here Φ_+ and Φ_- are matrices whose columns are the eigenvectors ϕ_n and φ_n, respectively.

2.1.1 Scattering matrix approach

The forward and backward amplitudes $\boldsymbol{a}_l$ and $\boldsymbol{b}_l$ are determined with aid of the scattering matrix $\hat{S}$, which relates the ingoing with the the outgoing waves in a physical system. Consider for instance the scattering of electromagnetic waves between the layers 0 and l (see Fig. 2.1), which is written as

$$\begin{pmatrix} \boldsymbol{a}_l \\ \boldsymbol{b}_0 \end{pmatrix} = \hat{S}(0,l) \begin{pmatrix} \boldsymbol{a}_0 \\ \boldsymbol{b}_l \end{pmatrix} = \begin{pmatrix} \hat{S}_{11}(0,l) & \hat{S}_{12}(0,l) \\ \hat{S}_{21}(0,l) & \hat{S}_{22}(0,l) \end{pmatrix} \begin{pmatrix} \boldsymbol{a}_0 \\ \boldsymbol{b}_l \end{pmatrix}. \tag{2.7}$$

In the same manner the scattering between layers l and N is expressed as:

$$\begin{pmatrix} \boldsymbol{a}_N \\ \boldsymbol{b}_l \end{pmatrix} = \begin{pmatrix} \hat{S}_{11}(l,N) & \hat{S}_{12}(l,N) \\ \hat{S}_{21}(l,N) & \hat{S}_{22}(l,N) \end{pmatrix} \begin{pmatrix} \boldsymbol{a}_l \\ \boldsymbol{b}_N \end{pmatrix}. \tag{2.8}$$

These two matrix equations allow us to obtain

$$\begin{aligned} \boldsymbol{a}_l &= [\hat{1} - \hat{S}_{12}(0,l)\hat{S}_{21}(l,N)]^{-1}[\hat{S}_{11}(0,l)\boldsymbol{a}_0 + \hat{S}_{12}(0,l)\hat{S}_{22}(l,N)\boldsymbol{b}_N], \\ \boldsymbol{b}_l &= [\hat{1} - \hat{S}_{21}(l,N)\hat{S}_{12}(0,l)]^{-1}[\hat{S}_{21}(l,N)\hat{S}_{11}(0,l)\boldsymbol{a}_0 + \hat{S}_{22}(l,N)\boldsymbol{b}_N], \end{aligned} \tag{2.9}$$

where the amplitudes $\boldsymbol{a}_0$ and $\boldsymbol{b}_N$ represent the incident waves in the system. We need to know the elements of $\hat{S}$ in order to obtain the field amplitudes. Then, we use the continuity of the field components parallel to the interface between two adjacent layers

$$\begin{pmatrix} \boldsymbol{e}_{||}(d_l) \\ \boldsymbol{h}_{||}(d_l) \end{pmatrix}_l = \begin{pmatrix} \boldsymbol{e}_{||}(0) \\ \boldsymbol{h}_{||}(0) \end{pmatrix}_{l+1},$$

which leads to the following relation

$$\begin{pmatrix} \hat{f}_l^+(d_l)\boldsymbol{a}_l \\ \boldsymbol{b}_l \end{pmatrix} = \hat{I}(l,l+1) \begin{pmatrix} \boldsymbol{a}_{l+1} \\ \hat{f}_{l+1}^-(d_{l+1})\boldsymbol{b}_{l+1} \end{pmatrix} = \begin{pmatrix} \hat{I}_{11} & \hat{I}_{12} \\ \hat{I}_{21} & \hat{I}_{22} \end{pmatrix} \begin{pmatrix} \boldsymbol{a}_{l+1} \\ \hat{f}_{l+1}^-(d_{l+1})\boldsymbol{b}_{l+1} \end{pmatrix}. \tag{2.10}$$

Here, $\hat{I}(l, l+1) = \hat{M}_l^{-1}\hat{M}_{l+1}$ is the interface matrix, which is associated with the crossing from one layer to the next one. On the other hand, the scattering process that occur between the layer l and another arbitrary layer l' are expressed as

$$\begin{pmatrix} \boldsymbol{a}_l \\ \boldsymbol{b}_{l'} \end{pmatrix} = \hat{S}(l', l) \begin{pmatrix} \boldsymbol{a}_{l'} \\ \boldsymbol{b}_l \end{pmatrix}, \tag{2.11}$$

Thus, from these two previous matrix equations, the following expression is achieved

$$\begin{pmatrix} -\hat{I}_{11} & \hat{f}_l^{+}\hat{S}_{12}\hat{S}_{22}^{-1} \\ -\hat{I}_{21} & \hat{S}_{22}^{-1} \end{pmatrix} \begin{pmatrix} \boldsymbol{a}_{l+1} \\ \boldsymbol{b}_{l'} \end{pmatrix} = \begin{pmatrix} -\hat{f}_l^{+}[\hat{S}_{11} - \hat{S}_{12}\hat{S}_{22}^{-1}\hat{S}_{21}] & \hat{I}_{12}\hat{f}_{l+1}^{-} \\ \hat{S}_{22}^{-1}\hat{S}_{21} & \hat{I}_{22}\hat{f}_{l+1}^{-} \end{pmatrix} \begin{pmatrix} \boldsymbol{a}_{l'} \\ \boldsymbol{b}_{l+1} \end{pmatrix},$$

which, after multiplying it from the left by the inverse of the left hand side matrix, leads the scattering matrix defined by

$$\begin{pmatrix} \boldsymbol{a}_{l+1} \\ \boldsymbol{b}_{l'} \end{pmatrix} = \begin{pmatrix} \hat{S}_{11}(l', l+1) & \hat{S}_{12}(l', l+1) \\ \hat{S}_{21}(l', l+1) & \hat{S}_{22}(l', l+1) \end{pmatrix} \begin{pmatrix} \boldsymbol{a}_{l'} \\ \boldsymbol{b}_{l+1} \end{pmatrix} = \hat{S}(l', l+1) \begin{pmatrix} \boldsymbol{a}_{l'} \\ \boldsymbol{b}_{l+1} \end{pmatrix}. \tag{2.12}$$

The 2×2 blocks of this matrix are given by

$$\begin{aligned}
\hat{S}_{11}(l', l+1) &= [\hat{I}_{11}(l, l+1) - \hat{f}_l^{+}(d_l)\hat{S}_{12}(l', l)\hat{I}_{21}(l, l+1)]^{-1}\hat{f}_l^{+}(d_l)\hat{S}_{11}(l', l), \qquad (2.13)\\
\hat{S}_{12}(l', l+1) &= [\hat{I}_{11}(l, l+1) - \hat{f}_l^{+}(d_l)\hat{S}_{12}(l', l)\hat{I}_{21}(l, l+1)]^{-1} \\
&\quad \times[-\hat{I}_{12}(l, l+1) + \hat{f}_l^{+}(d_l)\hat{S}_{12}(l', l)\hat{I}_{22}(l, l+1)]\hat{f}_{l+1}^{-}(d_{l+1}), \\
\hat{S}_{21}(l', l+1) &= \hat{S}_{22}(l', l)\hat{I}_{21}(l, l+1)\hat{S}_{11}(l', l+1) + \hat{S}_{21}(l', l), \\
\hat{S}_{22}(l', l+1) &= \hat{S}_{22}(l', l)\hat{I}_{21}(l, l+1)\hat{S}_{12}(l', l+1) + \hat{S}_{22}(l', l)\hat{I}_{22}(l, l+1)\hat{f}_{l+1}^{-}(d_{l+1}).
\end{aligned}$$

Starting from $\hat{S}(l', l') = \hat{1}$, one can apply the previous recursive relations to a layer at a time to build up $\hat{S}(l', l)$.

Reflection amplitude

We have completely determined the fields thorough the structure (see Eq. (2.5)). We can use them to obtain the reflection matrix

$$\begin{pmatrix} E_{x,0}^{(r)} \\ E_{y,0}^{(r)} \end{pmatrix} = \hat{R}_0 \begin{pmatrix} E_{x,0}^{(i)} \\ E_{y,0}^{(i)} \end{pmatrix} = \begin{pmatrix} (\hat{R}_0)_{11}E_{x,0}^{(i)} & (\hat{R}_0)_{12}E_{y,0}^{(i)} \\ (\hat{R}_0)_{21}E_{x,0}^{(i)} & (\hat{R}_0)_{22}E_{y,0}^{(i)} \end{pmatrix}, \tag{2.14}$$

where $E_{j,0}^{(i)}$ ($E_{j,0}^{(r)}$) denotes the field components of the incident (reflected) wave at the layer 0 (see Fig. 2.1). The reflection amplitude coefficients are written as

$$(\hat{R}_0)_{11} = \frac{E_{x,0}^{(r)}}{E_{x,0}^{(i)}} = \frac{M_{0,23}b_{0,1} + M_{0,24}b_{0,2}}{M_{0,21}a_{0,1} + M_{0,22}a_{0,2}}, \tag{2.15}$$

$$(\hat{R}_0)_{21} = \frac{E_{y,0}^{(r)}}{E_{x,0}^{(i)}} = -\frac{M_{0,13}b_{0,1} + M_{0,14}b_{0,2}}{M_{0,21}a_{0,1} + M_{0,22}a_{0,2}}, \tag{2.16}$$

where the amplitude $a_{0,1} = -\frac{M_{0,12}}{M_{0,11}}a_{0,2}$ and $a_{0,2} = 1$. Similarly,

$$(\hat{R}_0)_{12} = \frac{E_{x,0}^{(r)}}{E_{y,0}^{(i)}} = -\frac{M_{0,23}b_{0,1} + M_{0,24}b_{0,2}}{M_{0,11}a_{0,1} + M_{0,12}a_{0,2}}, \tag{2.17}$$

$$(\hat{R}_0)_{22} = \frac{E_{y,0}^{(r)}}{E_{y,0}^{(i)}} = \frac{M_{0,13}b_{0,1} + M_{0,14}b_{0,2}}{M_{0,11}a_{0,1} + M_{0,12}a_{0,2}}, \tag{2.18}$$

with $a_{0,2} = -\frac{M_{0,21}}{M_{0,22}}a_{0,1}$ and $a_{0,2} = 1$. Notice that reflection matrix defined in Eq. (2.14) is actually in the xy basis. Then, it must be changed to the sp basis, as in the previous section

$$\begin{aligned} r_{ss} &= (\hat{R}_0)_{22}, \\ r_{ps} &= (\hat{R}_0)_{21}, \\ r_{pp} &= (\hat{R}_0)_{11}, \\ r_{sp} &= (\hat{R}_0)_{12}, \end{aligned} \tag{2.19}$$

where θ is the angle of incidence.

Chapter 3

Enhancement of the Transverse Magneto-Optical Kerr Effect

Contents

The MO activity of a system is the result of the combined effects of the pure optical and MO properties of the global structure. In the case of the TMOKE which depends on the p-reflected amplitude, TMOKE $= \frac{R_{\mathrm{pp}}(+\mathbf{M})-R_{\mathrm{pp}}(-\mathbf{M})}{R_{\mathrm{pp}}(+\mathbf{M})+R_{\mathrm{pp}}(-\mathbf{M})}$, can reach high values if the R_{pp} coefficient tends to zero, and the excitation of surface-plasmon polaritons (SPPs) is a way to achieve it. The excitation of SPPs usually induces minima in the magnitudes corresponding to the pure optical contribution, as for example is the case of the excitation of SPPs using a Kretschmann[1] configuration, where a minimum in the reflectivity is the signature of plasmon excitation. In this specific case, the minimum value of pure optical contribution has as a direct consequence of a maximum in the TMOKE. However, the Kretschmann geometry to excite SPPs show some problems that make it difficult in the miniaturization process and development of modern devices.[22] For this reason, it is desirable to find new ways to enhance the TMOKE. Recently, some works have demonstrated the strong reduction of the wavevector in the indium-tin-oxide (ITO) below that of free space enabling the excitation of SPPs without requiring a prism or grating coupler. On the other hand, it has been very recently demonstrated that the resonant tunneling effects in trilayers with subwavelength widths, in the presence of realistic loss levels, are capable of yielding sensible Faraday rotation with transmittance levels that are an order of magnitude larger than those attainable with standalone slab

[1] It is one of the most used configuration for the excitation of surface plasmon polaritons. This consists of a prism with permittivity ε_p placed on a metal film (ε_m) with thickness d deposited on a dielectric substrate whit permittivity ε_s ($\varepsilon_s < \varepsilon_p$).

of MO metal of the same width.[16,17] Inspired by these works, we have reported two new proposals to enhance the TMOKE values, one of them is via resonant tunneling, in trilayer structures cointaining MO metals and the other one is through the coupling of ε-near-zero and surface plasmon polariton modes.[27,28] All these achievements are described in the next sections.

3.1 Enhancement of the TMOKE via resonant tunneling in tri-layers containing MO metals

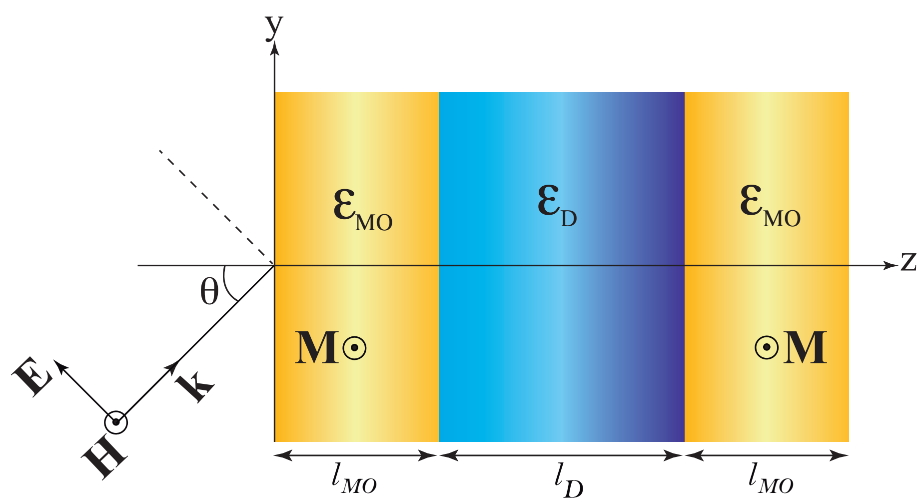

Figure 3.1: Schematic representation of the system under study. $\varepsilon_{\rm MO}$ and $\varepsilon_{\rm D}$, and $l_{\rm MO}$ and $l_{\rm D}$, are the corresponding dielectric permittivities and slab thicknesses for the MO and dielectric layers, respectively. *Figure taken from APL **109**, 033106 (2016).*

We have analysed a trilayer structure featuring a dielectric layer sandwiched between subwavelength width MO-metal layers, as depicted in Fig. 3.1. We show here that our concept, in the presence of realistic losses, allows to obtain giant TMOKE values in regions of very high transmissivity. It is worth no mention that by tuning the slab widths of the system, we may control the reflectivity, transmisivitty, and the TMOKE amplitudes, suggesting a way to develop compact and very simple magneto-optical devices which may be controlled by means of external applied magnetic fields.

In contrast with polar MO effects, which are related to the light polarization rotation, the TMOKE is a magneto-optical intensity effect which can be only observed when obliquely incident p-polarized light impinges over a system magnetized perpendicular to the incidence plane. This effect is characterized by the relative change on the amplitude of the reflected light when the magnetization of the system or an external applied magnetic field, **M**, is reversed (see Eq. 1.1)[50].

The transverse magnetization is confined to the plane parallel to the interfaces and perpendicular to the plane of incidence (see Fig. 3.1). The analysis is simpler than the polar and longitudinal configuration (see Fig. 1.2). This is due to the fact that, to first order in the off-diagonal element of the permittivity tensor, only the transversal magnetic wave (i.e., the wave polarized parallel, p, to the plane of incidence) is affected by the transverse magnetization. Here, we focus on analyse the reflection in a system consisting of a dielectric slab sandwiched between two magneto-optical metallic layers.

3.1.1 Transversal configuration

We have considered the plane of incidence as the yz plane and the magnetization is parallel to x axis. This allows to write the components of dielectric permittivity tensor as

$$\bar{\bar{\varepsilon}} = \begin{pmatrix} \varepsilon_{xx} & 0 & 0 \\ 0 & \varepsilon_{yy} & \varepsilon_{yz} \\ 0 & \varepsilon_{zy} & \varepsilon_{zz} \end{pmatrix}. \tag{3.1}$$

The proper polarization modes in this configuration can be split into two independent quadratic equations

$$[n_{zj}^{(n)2} - (\varepsilon_{xx} - n_y^2)] = 0, \tag{3.2a}$$

$$[\varepsilon_{zz} n_{zj}^{(n)2} + (\varepsilon_{yz} + \varepsilon_{zy}) n_y n_{zj}^{(n)} - \varepsilon_{yy}(\varepsilon_{zz} + n_y^2) + \varepsilon_{yz}\varepsilon_{zy}] = 0. \tag{3.2b}$$

The four solutions of the propagation vectors n_{zj}, with $j = 1, ..., 4$, are

$$n_{z1,2}^{(n)} = \pm(\varepsilon_{xx} - n_y^2)^{1/2}, \tag{3.3a}$$

$$n_{z3,4}^{(n)} = \frac{-n_y(\varepsilon_{yz} + \varepsilon_{zy}) \pm [n_y^2(\varepsilon_{yz} + \varepsilon_{zy})^2 + 4\varepsilon_{yy}(\varepsilon_{zz} - n_y^2) - 4\varepsilon_{yz}\varepsilon_{zy}\varepsilon_{zz}]^{1/2}}{2\varepsilon_{zz}}, \tag{3.3b}$$

where $j = 1, 2$ and $j = 3, 4$ correspond to the transversal electric ($-s$) and magnetic ($-p$) component of the wave, respectively. The corresponding proper polarizations of the eigen-values $n_{z1}^{(n)} = -n_{z2}^{(n)} = (\varepsilon_{yy} - n_x^2)^{1/2}$, are

$$\mathbf{e}_{1,2}^{(n)} = \begin{pmatrix} 1 \\ 0 \\ 0 \end{pmatrix}. \tag{3.4}$$

For the other pair, $n_{z3}^{(n)}$ and $n_{z4}^{(n)}$, we get

$$\mathbf{e}_{3,4}^{(n)} = \begin{pmatrix} 0 \\ \varepsilon_{zz} - n_y^2 \\ -n_y n_{z,3,4}^{(n)} - \varepsilon_{zy} \end{pmatrix}. \tag{3.5}$$

The corresponding magnetic field polarizations are written as

$$\mathbf{b}_{1,2}^{(n)} = \begin{pmatrix} 0 \\ n_{z1,2}^{(n)} \\ -n_y \end{pmatrix}, \tag{3.6}$$

for $n_{z1,2}^{(n)}$, whereas for $n_{z3}^{(n)}$ and $n_{z4}^{(n)}$, one obtains

$$\mathbf{b}_{3,4}^{(n)} = C_{3,4}^{(n)} \begin{pmatrix} -n_{z3,4}\varepsilon_{zz} - n_y \varepsilon_{zy} \\ 0 \\ 0 \end{pmatrix}. \tag{3.7}$$

From this information, we can construct the dynamical matrix for the transverse magnetization. It assumes a block diagonal form

$$\mathbf{D}^{(n)} = \begin{pmatrix} 1 & 1 & 0 & 0 \\ n_{z1} & -n_{z1} & 0 & 0 \\ 0 & 0 & \varepsilon_{zz} - n_y^2 & \varepsilon_{zz} - n_y^2 \\ 0 & 0 & -(n_y\varepsilon_{zy} + n_{z3}\varepsilon_{zz}) & -(n_y\varepsilon_{zy} + n_{z4}\varepsilon_{zz}) \end{pmatrix}. \tag{3.8}$$

As it can be seen from the above results Eqs. (3.5)-(3.7), only the p-component of light will be affected by the applied magnetic field, whereas the s-component does not experiment any variation. Taking into account that we have a tri-layer (see Fig. 3.1), the corresponding transfer matrix can be written as

$$\mathbf{T} = \mathbf{D}_0^{-1}\tilde{\mathbf{S}}_{\mathrm{MO}}\tilde{\mathbf{S}}_{\mathrm{D}}\tilde{\mathbf{S}}_{\mathrm{MO}}\mathbf{D}_0, \tag{3.9}$$

where $\mathbf{D}_0$ is the dynamical matrix for the background, $\tilde{\mathbf{S}}_{\mathrm{MO}}$ and $\tilde{\mathbf{S}}_{\mathrm{D}}$ are the characteristic matrices[51] for the MO metal and the central dielectric layer, respectively. Although these matrices can be found in the available literature[47,52], in order to be clear in our analytical procedure, we write them

$$\mathbf{D}_0 = \begin{pmatrix} 1 & 1 & 0 & 0 \\ \cos\theta & -\cos\theta & 0 & 0 \\ 0 & 0 & \cos\theta & \cos\theta \\ 0 & 0 & -1 & 1 \end{pmatrix}, \tag{3.10}$$

$$\tilde{\mathbf{S}}_{\mathrm{D}} = \begin{pmatrix} \cos(\beta_D) & i\frac{\sin(\beta_D)}{n_D} & 0 & 0 \\ in_D\sin(\beta_D) & \cos(\beta_D) & 0 & 0 \\ 0 & 0 & \cos(\beta_D) & -\frac{in_D\sin(\beta_D)}{\varepsilon_D} \\ 0 & 0 & -\frac{i\varepsilon_D\sin(\beta_D)}{n_D} & cos(\beta_D) \end{pmatrix}, \tag{3.11}$$

and $\tilde{\mathbf{S}}_{\mathrm{MO}}$

$$\tilde{\mathbf{S}}_{\mathrm{MO}} = \begin{pmatrix} S_{\mathrm{MO},1,1} & S_{\mathrm{MO},1,2} & 0 & 0 \\ S_{\mathrm{MO},2,1} & S_{\mathrm{MO},2,2} & 0 & 0 \\ 0 & 0 & S_{\mathrm{MO},3,3} & S_{\mathrm{MO},3,4} \\ 0 & 0 & S_{\mathrm{MO},4,3} & S_{\mathrm{MO},4,4} \end{pmatrix}, \tag{3.12}$$

where

$$S_{\mathrm{MO},1,1} = \cos(\beta_{\mathrm{MO},1}), \tag{3.13}$$

$$S_{\mathrm{MO},1,2} = \frac{i\sin(\beta_{\mathrm{MO},1})}{n_{z1}}, \tag{3.14}$$

$$S_{\mathrm{MO},2,1} = in_{z1}\sin(\beta_{MO,1}), \tag{3.15}$$

$$S_{\mathrm{MO},2,2} = S_{\mathrm{MO},1,1}, \tag{3.16}$$

$$S_{\mathrm{MO},3,3} = \cos(\beta_{\mathrm{MO},3}) - \frac{in_y\varepsilon_{zy}\sin(\beta_{\mathrm{MO},3})}{n_{z3}\varepsilon_0}, \tag{3.17}$$

$$S_{\mathrm{MO},3,4} = \frac{i\left(n_y^2-\varepsilon_0\right)\sin(\beta_{\mathrm{MO},3})}{n_{z3}\varepsilon_0}, \tag{3.18}$$

$$S_{\mathrm{MO},4,3} = i\frac{(n_{z3}^2\varepsilon_0^2 - n_y^2\varepsilon_{zy}^2)\sin(\beta_{\mathrm{MO},3})}{n_{z3}\left(n_y^2-\varepsilon_0\right)\varepsilon_0}, \tag{3.19}$$

$$S_{\mathrm{MO}4,4} = \cos(\beta_{\mathrm{MO},3}) + \frac{in_y\varepsilon_{zy}\sin(\beta_{\mathrm{MO},3})}{n_{z2}\varepsilon_0}, \tag{3.20}$$

with $n_y = n_{\mathrm{B}}\sin\theta$, where $n_B = 1$ is the refractive index for the background material (air in this case), and θ corresponds to the angle of incidence. The respective components of the dielectric permittivity can be written as $\varepsilon_{xx} = \varepsilon_{yy} = \varepsilon_{zz} = \varepsilon_0$ for diagonal and $\varepsilon_{yz} = -\varepsilon_{zy} = i\varepsilon_1$ for the off-diagonal elements[47,52]. From here on, we will consider the working wavelength as $\lambda = 631$ nm. Then, in order to work with realistic parameter values we take $\varepsilon_0 = -10.51+2.1i$, $\varepsilon_1 = -1.2+1.15i$ for the MO metallic layers[53], corresponding to the Co_6Ag_{94} material measured at room temperature after annealing at 250 °C. For the central dielectric layer we consider an isotropic permittivity as $\varepsilon_{\mathrm{D}} = 2.12$, corresponding to the dielectric material SiO_2[54] in the case of our working wavelength. For Eqs. (3.13)-(3.20) we have used: $\beta_{\mathrm{MO},1} = 2\pi n_{z1}\frac{l_{\mathrm{MO}}}{\lambda}$, $\beta_{\mathrm{MO},3} = 2\pi n_{z3}\frac{l_{\mathrm{MO}}}{\lambda}$, $n_{z1} = \sqrt{\varepsilon_0 - n_y^2}$, $n_{z3} = \sqrt{\varepsilon_0 - n_y^2 + \frac{\varepsilon_{yz}^2}{\varepsilon_0}}$, $\beta_D = 2\pi n_D\frac{l_D}{\lambda}$, and $n_D = \sqrt{\varepsilon_{\mathrm{D}} - n_y^2}$.

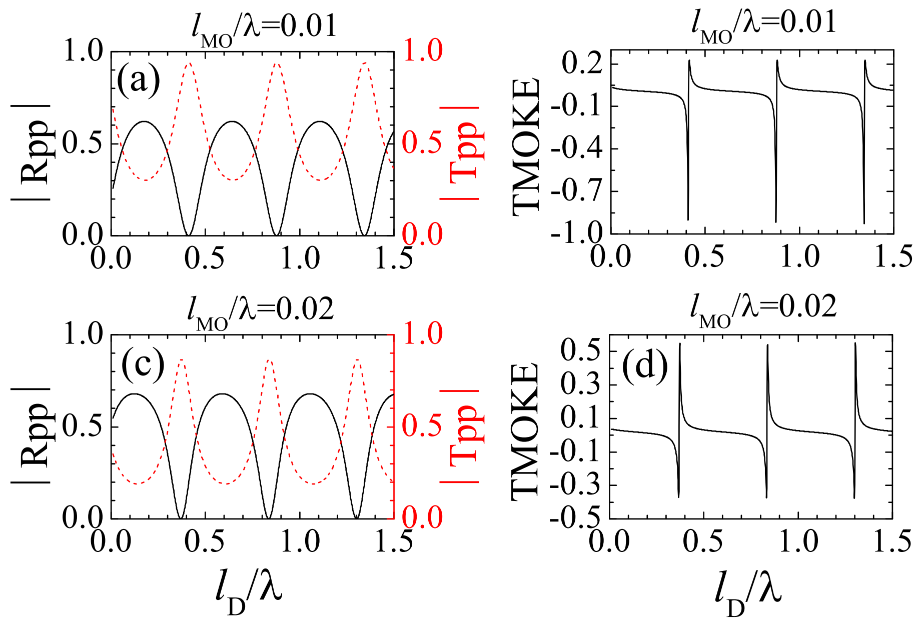

Figure 3.2: Reflection (solid lines in left panel), transmission (dashed lines in left panel), and TMOKE (right panel) amplitudes for different MO slab thicknesses. The upper panel is for $l_{\mathrm{MO}}/\lambda = 0.01$ and the lower one corresponds to $l_{\mathrm{MO}}/\lambda = 0.02$. The angle of incidence was considered as $\theta = 80°$. *Figure taken from APL* ***109****, 033106 (2016).*

3.1.2 Contribution of the Resonant tunnelling modes

In the left panel of Fig. 3.2 we show the transmission (dotted lines) and reflection (solid lines) spectra of p-polarized waves for two different l_{MO}-widths, as function of l_{D}/λ, without magnetic effects. The corresponding TMOKE amplitudes when an external applied magnetic field, or the magnetization in the MO slabs, is reversed from $+\mathbf{M}$ to -$\mathbf{M}$ is shown in the right panel of Fig. 3.2 for both l_{MO}-widths. From these results we may see that the transmission amplitude diminishes as the l_{MO}-width increases, indicating that near perfect transmission can be only found in the region of very thin MO slabs, in agreement with previous reports.[17] On the other hand, we may observe that TMOKE amplitude have non-zero values only around the resonance transmission peaks. Furthermore, we can observe that TMOKE reaches extraordinary values, near 1.0, only for $l_{\mathrm{D}}/\lambda = 0.01$, where transmission at the corresponding resonances is around 0.95, while for $l_{\mathrm{D}}/\lambda = 0.02$ the maximum TMOKE diminishes, but remains strongly enhanced with values around 0.4, i.e., enhanced by two orders of magnitude. In order to understand such a behavior, in Fig. 3.3 we have plotted the reflection spectra R_{pp}(-$\mathbf{M}$)

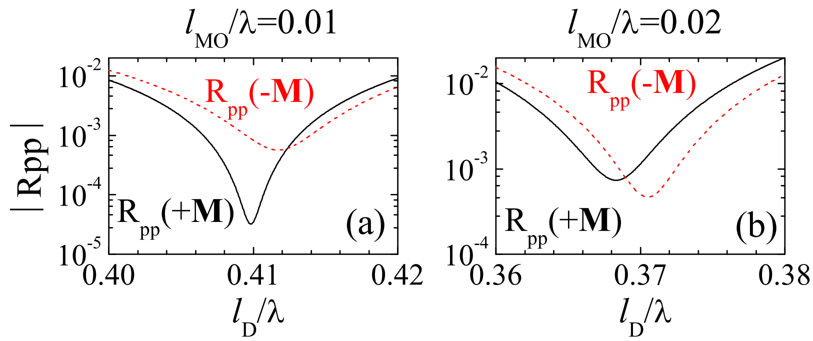

Figure 3.3: Amplitudes of the reflection spectra $\mathrm{R_{pp}}$, around the corresponding first resonant transmission peak from Fig. 3.2, as function of l_{D}/λ. Solid and dashed lines correspond to $\mathrm{R_{pp}}$(-**M**) and $\mathrm{R_{pp}}$(+**M**), respectively. *Figure taken from APL* ***109****, 033106 (2016).*

and $\mathrm{R_{pp}}(+\mathbf{M})$ for two different l_{MO}-thicknesses, as function of l_{D}/λ. From this latter figure we can observe that both reflection spectra, $\mathrm{R_{pp}}$(-**M**) and $\mathrm{R_{pp}}(+\mathbf{M})$, near the perfect transmission resonance are very different in magnitude. From Fig. 3.3(a), for $l_{\mathrm{D}}/\lambda = 0.01$, we can see that around the resonance $\mathrm{R_{pp}}(+\mathbf{M})\sim 0.001$, while $\mathrm{R_{pp}}$(-**M**) reaches negligible values of the order of $\sim 10^{-7}$. Such a difference on both reflections is due to the changes on the boundary conditions, at the MO interfaces, induced by the magnetic field effects. On the other hand, from Fig. 3.3(b) we may note that both reflections become comparable in magnitude but shifted around the corresponding resonances as l_{MO} increases, which explain the diminishing on the amplitude and the oscillation of the TMOKE observed in Fig. 3.2(d). We believe such changes on the corresponding reflection spectra are intimately related to the increasing on the absorbance spectra as l_{MO} increases, which may be seen by comparing the transmission and reflection spectra from Figs. 3.2(a), 3.2(c) and 3.5(a). With previous results Figs. (3.2)-(3.3), we can affirm that the resonant tunneling modes are the responsible of the enhancement of the TMOKE through the structure. Thus, we are going to calculate them using the transfer matrix method Eqs. (3.9)-(3.12). The transversal magnetic reflection coefficient is defined as

$$r_{pp} = \frac{\mathbf{T}_{4,3}}{\mathbf{T}_{3,3}}. \tag{3.21}$$

For the existence of resonant tunneling modes, it is necessary that the condition $\mathbf{T}_{4,3} = 0$ be fulfilled, ensuring that the electromagnetic wave passes through the entire structure without presenting information loss by reflection. We have then

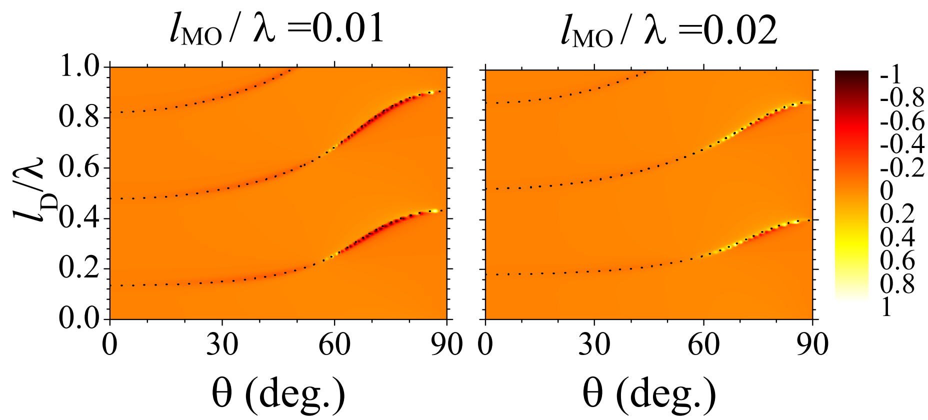

Figure 3.4: TMOKE as function of l_D/λ and θ for two l_{MO} thicknesses. Dotted lines correspond to the analytical solutions for the resonant transmission from Eq. (3.25). Results are for $\lambda = 631$ nm. *Figure taken from APL **109**, 033106 (2016).*

$$\mathbf{T}_{4,3} = A\cos(\beta_d) + B\sin(\beta_d) = 0, \tag{3.22}$$

with

$$\begin{aligned} A &= n_D(S_{MO,3,3} + S_{MO,4,3})\varepsilon_D\left(-S_{MO,3,4} + S_{MO,4,3}\right. \\ &+ \left. 2(S_{MO,3,3} - S_{MO,4,3})\cos\theta + S_{MO,4,3}\cos 2\theta\right), \end{aligned} \tag{3.23}$$

$$\begin{aligned} B &= 2i\cos\theta\left(-S_{MO,4,3}(n_D^2 S_{MO,4,3} + S_{MO,3,3}\varepsilon_D^2)\right. \\ &- (S_{MO,3,3} - S_{MO,4,3})(n_D^2 S_{MO,4,3} + S_{MO,3,4}\varepsilon_D^2)\sec\theta \\ &+ \left.(n_D^2 S_{MO,3,3}S_{MO,4,3} + S_{MO,3,4}^2\varepsilon_D^2)\sec^2\theta\right). \end{aligned} \tag{3.24}$$

Isolating β_d of the Eq. (3.22), we can obtain the relation of the resonant tunneling for different thickness of the dielectric layer

$$\frac{l_D}{\lambda} = \frac{1}{2\pi n_D}\arctan\left(-\frac{B}{A} + m\pi\right). \tag{3.25}$$

In Figs. 3.4(a)-(b) we plot the TMOKE as function of θ and l_D for $l_{MO}/\lambda = 0.01$ and $l_{MO}/\lambda = 0.02$, respectively. Dotted lines depict the analytical solutions from Eq. (3.25). From these results we may clearly observe that the maximum TMOKE values are found along the resonant tunneling condition, for each θ and l_D, following also the periodic behavior of these resonant solutions predicted from Eq. (3.25). Furthermore, it can be directly observed from these results that there would be a value of θ from which the maximum TMOKE values are reached, in the present case we have $\theta > 60°$.

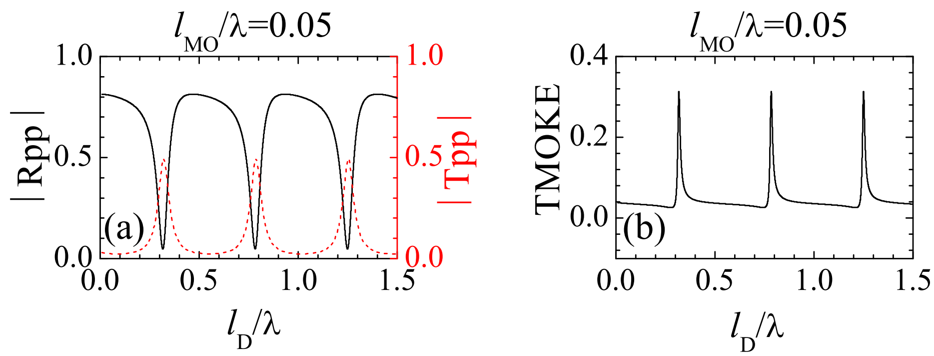

Figure 3.5: Reflection (solid line in left panel), transmission (dashed line in left panel), and TMOKE (right panel) amplitudes for $l_{\mathrm{MO}}/\lambda = 0.05$. Results were obtained by considering $\theta = 80°$ and $\lambda = 631$ nm. *Figure taken from APL **109**, 033106 (2016).*

Such a behavior of the TMOKE with θ can be qualitatively understood in terms of the enhancement of the light-bulk-plasma coupling as the longitudinal component of **E** increases, which in turn leads to an increasing on the magnitude of the Lorentz force over the electrons in the MO metal layers. The corresponding diminishing on the TMOKE amplitude as l_{MO} increases was explained above as an increasing in the losses on the system.

Results up to here have been only obtained within the low reflectivity region ($\mathrm{R_{pp}} \sim 0.001$), making the TMOKE measurements only available for high sensitive reflectometers. In order to deal with this issue we may tailor the MO slabs widths in order to tune the reflection amplitude to a greater value, but retaining a relatively high transmissivity, as may be observed from Fig. 3.5. In this latter figure we show the corresponding transmission, reflection, and TMOKE spectra as function of l_{D}/λ for a system with $l_{\mathrm{MO}}/\lambda = 0.05$, from where we may observe a reflectivity around 0.05 with the corresponding transmissivity near 0.5, while the TMOKE reaches magnitudes near 0.17 at these resonances, thus retaining an enhancement by two orders of magnitude.

Another interesting feature we have observed is the odd angular symmetry of the TMOKE, i.e., for each pair of incident angles with opposite signs, $+\theta$ and $-\theta$, the TMOKE spectra have opposite signs, as it may be observed from Fig. 3.6. The same feature was experimentally observed in a recent work[15] related with the resonant enhancement of the TMOKE by means of the waveguide-plasmon-polariton excitation. We think this odd symmetry of the TMOKE for each pair of incident angles with opposite signs can be understood as due to the change of sign on the component of **E** along the z-axis, which alter the sense of the light-plasma oscillation, and thus the sign of the corresponding Lorentz forces for +**M** and -**M**, respectively.

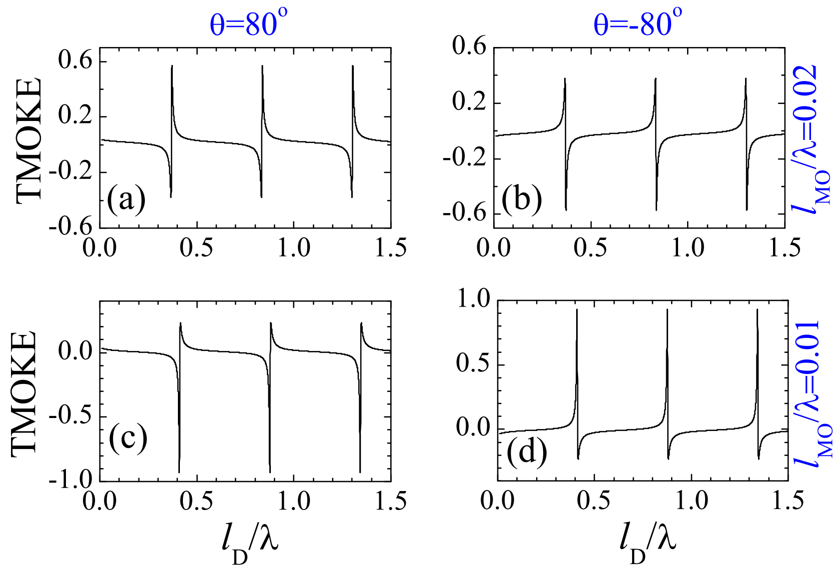

Figure 3.6: (Color online) TMOKE amplitudes in the regions of (a)-(b) low and (c)-(d) high transmissivity for a pair of incident angles with opposite signs, $+\theta$ and $-\theta$, in order to evidence the odd angular symmetry of the TMOKE in trilayer systems. For the calculations we have considered $\theta = 80^\circ$ with $\lambda = 631$ nm. *Figure taken from APL* ***109****, 033106 (2016).*

3.2 Giant enhancement of the TMOKE through the coupling of ε-near-zero and surface plasmon polariton modes

Recently, Traviss *et. al*. showed experimentally[23] the excitation of SPP resonances without the use of a prism or grating coupler. They controlled light absorption in nanostructured indium tin oxide (ITO) films operating in the ε-near-zero (ENZ) frequency regime.[24–26] Such excitation was reached through the coupling of the perfect absorbing ENZ-mode[55] at the ENZ slab with the allowed SPP mode at the ENZ/Metal interface for p-polarized incident light.

We demonstrated theoretically[28] that the direct coupling of SPP can be further exploited to obtain a giant enhancement of TMOKE, with amplitudes reaching the maximum theoretical values of ± 1. The concept is based on the use of a MO ENZ structure for magnetic modulation of SPP resonances while simultaneously maintaining a high level of absorbance. We show that it is possible to obtain the giant enhancement of TMOKE by using a hypothetical MO ENZ slab grown over a gold substrate. The vanishing behavior in the dielectric permittivity of the hypothetical slab, responsible for the giant enhancement of TMOKE, is carefully selected to occur at the near-infrared region. This choice was made because we propose later on in this document a feasible structure with an ITO slab as the ENZ material that can show this effect experimentally. ITO films can be built[56–58] with thicknesses ranging from $\sim$ 4 nm to $\sim$ 600 nm to have electron densities in between that of noble metals (10^{22} cm^{-3}) and doped semiconductors (10^{19} cm^{-3}). Also, significant tuning of the electron density of ITO films can be made with electrical or optical methods,[59] allowing its use in near-infrared optical modulators and sensing devices.[60,61]

Let us first discuss the case of a hypothetical MO ENZ slab with thickness l and dielectric permittivity tensor given by

$$\varepsilon_{xx} = \varepsilon_{yy} = \varepsilon_{\|} = 5.8 - \frac{0.2\nu_{\mathrm{p}}^2}{\nu^2 + i\nu\gamma_0}, \tag{3.26}$$

$$\varepsilon_{zz} = = \varepsilon_{\perp} = 7.81 - \frac{2.19\left(\nu^2 + i\nu\gamma_0\right)}{\nu^2 + i\nu\gamma_0 - 0.18\nu_{\mathrm{p}}^2}, \tag{3.27}$$

$$\varepsilon_{xz} = -\varepsilon_{zx} = 0.048i, \tag{3.28}$$

where $\nu_{\mathrm{p}} = 0.477$ PHz and $\gamma_0 = 4.775 \times 10^{-3}$PHz, with subindices $\|$ and $\perp$ indicating components parallel and normal to the xy-plane. The incidence plane is the xz-plane, the magnetization of the MO ENZ slab is considered normal to the growth-direction, z-axis, and parallel to the y-axis. Around the frequency $\nu_{\perp} = 0.2385$ PHz, $\varepsilon_{\perp} \approx 0$, since at this frequency there is a transition from negative to positive values for the real part of permittivity, *i.e.*, $\mathrm{Re}\{\varepsilon_{\perp}(\nu_{\perp})\} = 0$. Along this document we will use a fixed working wavelength at the near-infrared corresponding to $\lambda_0 = 1229$ nm.

For simplicity, in the analytical treatment we define $\widehat{\eta} = \widehat{\varepsilon}^{-1}$. Thus

$$\widehat{\eta} = \begin{pmatrix} \eta_{xx} & 0 & \eta_{xz} \\ 0 & \eta_{yy} & 0 \\ \eta_{zx} & 0 & \eta_{zz} \end{pmatrix}, \tag{3.29}$$

with

$$\widehat{\eta} = (\varepsilon_{||}\varepsilon_{\perp} + \varepsilon_{xz}^2)^{-1} \begin{pmatrix} \varepsilon_{\perp} & 0 & -\varepsilon_{xz} \\ 0 & (\varepsilon_{||}\varepsilon_{\perp} + \varepsilon_{xz}^2)/\varepsilon_{||} & 0 \\ \varepsilon_{xz} & 0 & \varepsilon_{||} \end{pmatrix}, \tag{3.30}$$

from which we calculate the eigenvector corresponding to p-polarized incident light, with $\omega = 2\pi\nu$, as

$$q_p = \sqrt{\frac{\omega^2}{c^2}\frac{1}{\eta_{xx}} - k_x^2\frac{\eta_{zz}}{\eta_{xx}}}. \tag{3.31}$$

For the incident medium or gold substrate we use $q_i = \sqrt{\frac{\omega^2}{c^2}\frac{1}{\eta_i} - k_x^2}$, with i being 0 or Au, respectively. From now on, we use $q_{\mathrm{ENZ}} = q_p$ for simplicity in discussing the

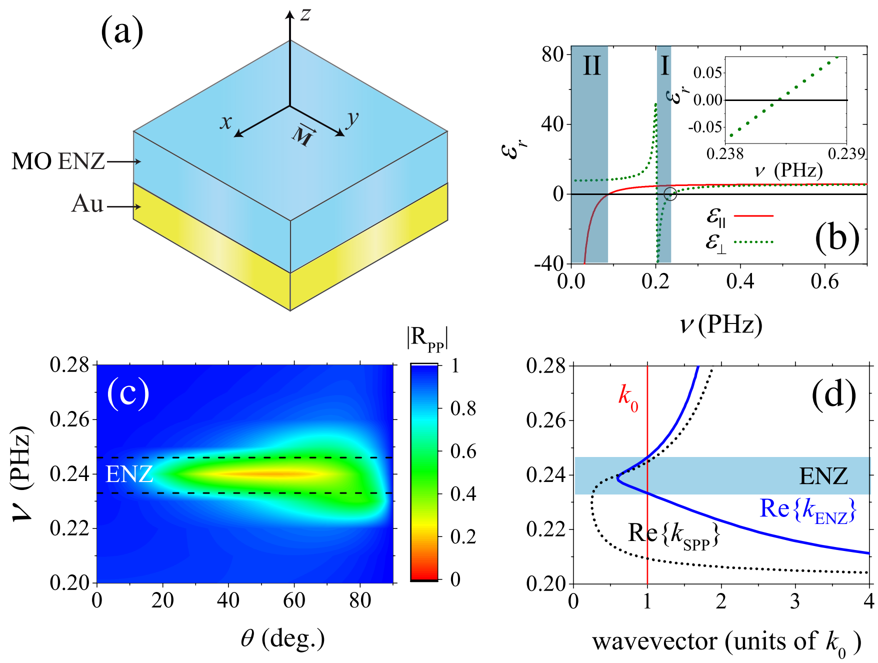

Figure 3.7: (a) Schematic representation of the system under study. (b) Permittivities parallel and normal to the plane of magnetization for the hypothetical ENZ slab. The inset shows a zoom of the permittivity around their zero value. (c) Reflectance as a function of frequency and incident angle θ, for a MO ENZ slab thickness l = 159.77 nm, calculated by using the SMM. Horizontal dashed lines are used to depict the ENZ region. (d) Numerical solutions for the real part of the wavevectors, along the x-axis, in air (k_0), SPPs at ENZ/gold interface (k_{SPP}), and perfect absorbing modes (k_{ENZ}). *Figure taken from PRB **96**, 075415 (2017).*

results. The conditions for the excitation of perfectly absorbing (PA) ENZ modes and SPP resonances, for the system in Fig. 3.7, can be obtained from SMM for anisotropic media[48,49] as

$$e^{2iq_{\mathrm{ENZ}}d} = \frac{(q_0\eta_0 - q_{\mathrm{ENZ}}\eta_{xx} + k_x\eta_{xz})(q_{\mathrm{Au}}\eta_{\mathrm{Au}} + q_{\mathrm{ENZ}}\eta_{xx} + k_x\eta_{xz})}{(q_0\eta_0 + q_{\mathrm{ENZ}}\eta_{xx} + k_x\eta_{xz})(q_{\mathrm{Au}}\eta_{\mathrm{Au}} - q_{\mathrm{ENZ}}\eta_{xx} + k_x\eta_{xz})}, \tag{3.32}$$

and

$$\tan\left(q_{\mathrm{ENZ}}d\right) = \frac{-iq_{\mathrm{ENZ}}\left(q_0\eta_0 + q_{\mathrm{Au}}\eta_{\mathrm{Au}}\right)\eta_{xx}}{q_{\mathrm{Au}}q_0\eta_0\eta_{\mathrm{Au}} + \left(q_0\eta_0 - q_{\mathrm{Au}}\eta_{\mathrm{Au}}\right)k_x\eta_{xz} + \left(q_{\mathrm{ENZ}}\eta_{xx}\right)^2 - \left(k_x\eta_{xz}\right)^2}, \tag{3.33}$$

respectively, where q_0, q_{Au}, and q_{ENZ} correspond to the wavevectors in air, gold and

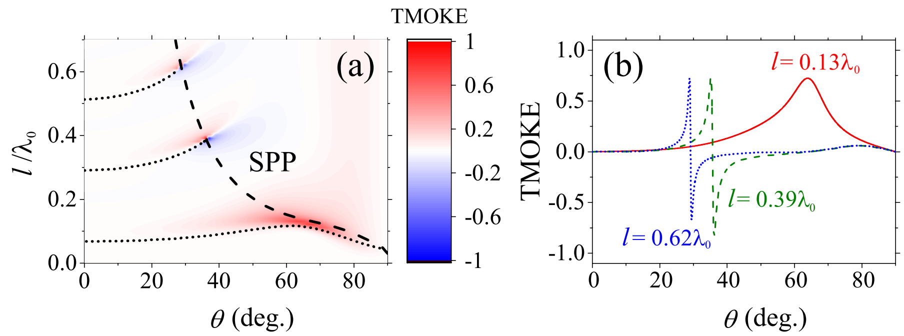

Figure 3.8: (a) TMOKE as a function of the angle of incidence and thickness, l/λ_0, of the MO ENZ slab for a working wavelength $\lambda_0 = 1229$ nm. The dotted and dashed lines indicate the perfectly absorbing (PA) ENZ and SPP modes, from Eqs. (3.32) and (3.33), respectively. (b) TMOKE for three thicknesses of the effective MO ENZ slab. *Figure taken from PRB **96**, 075415 (2017).*

ENZ slab. k_{ENZ} and k_{SPP} are obtained by solving k_x from the above equations for each case.

Fig. 3.7 depicts the system under study with its permittivity (ε) and reflectivity (R_{pp}) as functions of the frequency and angle of incidence, θ, around the ENZ region. The corresponding dispersion relations $\mathrm{Re}\{k_{\mathrm{ENZ}}\}$, $k_0 = \omega/c$ and $\mathrm{Re}\{k_{\mathrm{SPP}}\}$ are also plotted. The absorbance is usually defined as $A = 1 - R - T$, where R and T correspond to the reflectance and transmittance, respectively. In the present case, the absorbance becomes $A = 1 - R$ as the ENZ slab is backed by a metallic substrate, thus yielding an effectively zero transmittance. A range of θ-values with negligible reflectance, *i.e.*, very high absorbance, are observed in Fig. 3.7(c) within the ENZ region. Such behavior can be explained in terms of the strong electromagnetic field localization due to the excitation of the ENZ-mode in the ENZ slab.[24–26] According to the dispersion relations in Fig. 3.7(d), the wavevector k_{ENZ} along the x-axis can match k_{SPP} in the ENZ region, thus allowing for coupling of the ENZ and SPP modes without a prism or grating coupler.[23]

Fig. 3.8(a) shows that giant TMOKE values can only be obtained when PA ENZ modes are very close or match the SPP resonances, *i.e.*, when a coupling of ENZ-SPP modes occurs. Strongly enhanced TMOKE values appear only when strong absorption is linked to excitation of SPP resonances, as indicated in Figs. 3.9(a)-(d). It is significant that reflectance values of the order of 10^{-4} have been measured in related experiments,[62] but measuring lower values as obtained in our work may be challenging. The coupling of ENZ modes to other types of modes has been demonstrated; for example, the strong optical coupling in an ENZ material-semiconductor hybrid structure is suitable for a

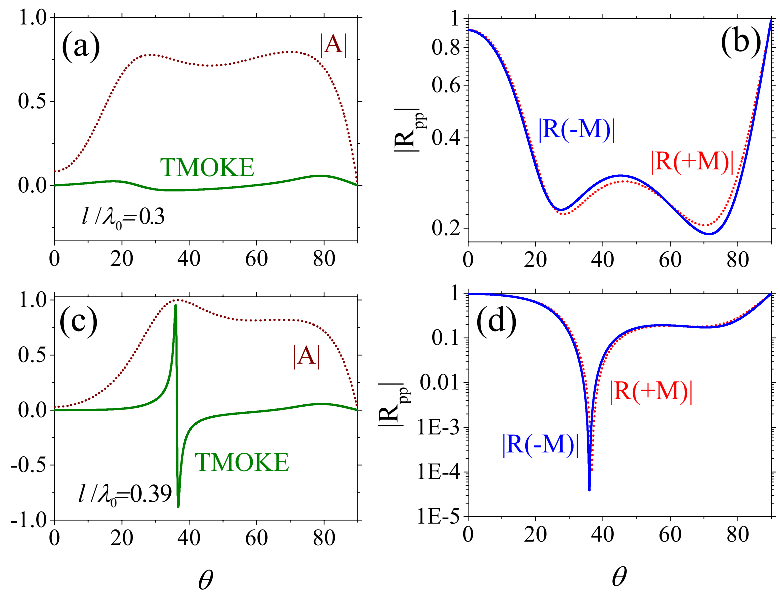

Figure 3.9: (a)-(b) and (c)-(d) show the absorption, TMOKE, $R_{pp}(+\mathbf{M})$ and $R_{pp}(-\mathbf{M})$, for $l/\lambda_0 = 0.3$ and $l/\lambda_0 = 0.39$, respectively. The dotted and solid lines in (a) and (c) correspond to the absorption and TMOKE, respectively. High absorbances with low TMOKE values are observed for $l/\lambda_0 = 0.3$, in comparison with the corresponding PA ENZ solution in Fig. 3.2(a) in the main text, while giant TMOKE values are obtained at the intersection of PA ENZ and SPP modes for $l/\lambda_0 = 0.39$. *Figure taken from PRB **96**, 075415 (2017).*

highly tunable integrated device.[63] For quasi-matching of PA ENZ with SPP modes, broad giant TMOKE peaks appear, in contrast to perfect coupling where TMOKE curves are very sharp, as seen in Fig. 3.8(b).

An experimentally feasible system to observe giant TMOKE values due to coupling of PA ENZ with SPP modes is depicted in Fig. 3.10(a). The platform is designed as a trilayer arrangement of ITO/BIG-YIG/SiO_2 grown over a gold substrate, which can be developed with available experimental techniques.[64,65] In this platform, the ITO slab is responsible for the ENZ behavior, while the BIG:YIG slab contributes with MO effects and SiO_2 and Au serve as the substrate. The ITO layer is described by an isotropic permittivity $\varepsilon_{\mathrm{ITO}} = \varepsilon_\infty - \frac{\nu_\mathrm{p}^2}{\nu^2 + i\gamma\nu}$, where $\gamma = 0.03$ PHz and $\nu_\mathrm{p} = 0.477$ PHz denote the damping rate and plasma frequency. We used $\varepsilon_\infty = 4$, $m^* = 0.4m_\mathrm{e}$ and $N = 1.13 \times 10^{21}$ cm^{-3} for the high-frequency permittivity, effective mass and carrier density, respectively, taken from experimental values in Ref. [23]. Parameters for BIG-YIG were taken from Refs. [42,66]. The TMOKE curves obtained as a function of θ in Fig. 3.10(b) change significantly when the refractive index (RI) of the incident medium is varied, which occurs even for very small changes. Fig 3.10(c) shows

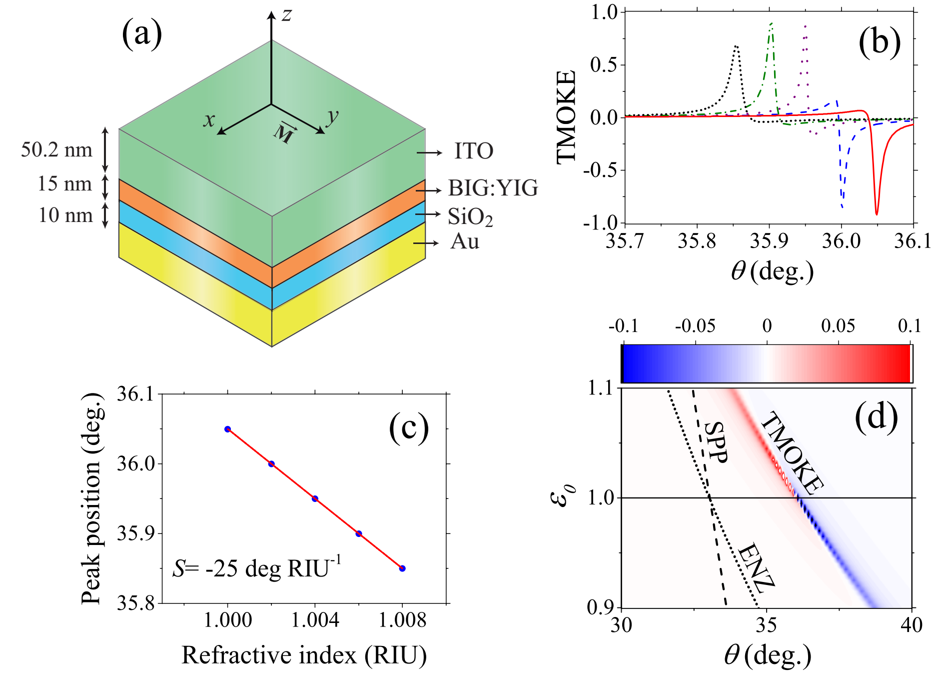

Figure 3.10: Pictorial view of the multilayer system on a gold substrate. (b) TMOKE as a function of the incident angle for five values of RI. Solid, dashed, dotted, dash-dotted and dot-dotted lines are for RI values of 1.000, 1.002, 1.004, 1.006, and 1.008, respectively. (c) TMOKE peak position as a function of RI, showing a linear behavior with slope $S = -25$ deg.$\cdot$RIU^{-1}. (d) TMOKE as a function of the dielectric permittivity of the incident medium, ε_0, and angle of incidence. The dashed and dotted lines show the solutions for SPP and ENZ modes when the system is considered as an effective medium. *Figure taken from PRB **96**, 075415 (2017).*

that θ for the maximum amplitude of TMOKE in Fig. 3.10(b) varies linearly with the change in RI, with a slope $S = -25°/\text{RIU}$. Since ITO films may be functionalized with phosphonates,[67] amines,[68] zirconium complexes,[69] carboxylic acids and thiols,[70] DNA,[71] and silanes,[72] the results in Fig. 3.10 can be exploited, for example, in designing novel sensing/biosensing platforms to detect or monitor very small RI changes in the incident medium, with high precision. Significantly, the S value is of the same order of magnitude as in a recent Kretschmann-based SPR sensor for detecting glucose.[73] Fig. 3.10(d) shows the TMOKE, from -0.1 to 0.1 (for visual purposes), as a function of the incident medium dielectric permittivity, ε_0, and incident angle, θ, from which a change of sign is clearly observed. A qualitative interpretation of this sign alternation can be given by considering the trilayer system as just one effective medium (similar to the basic case shown in Fig. 3.7) to calculate the corresponding SPR and ENZ modes shown by the dashed and solid lines in Fig. 3.10(d), respectively.

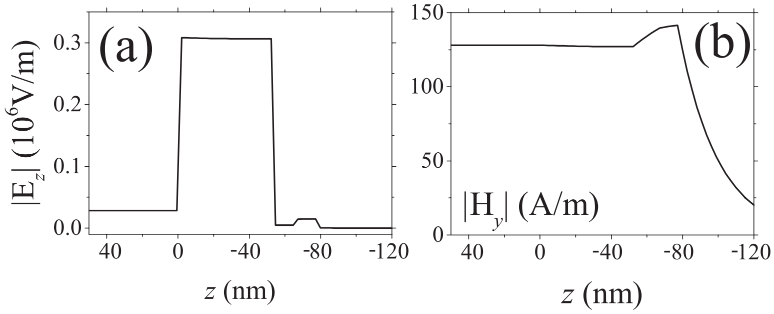

Figure 3.11: (a) electric, E_z, and (b) magnetic, H_y, fields along the multilayer structure for light impinging with an incident angle $\theta = 36°$. In (a) E_z is strongly localized at the ITO layer. The net enhancement of TMOKE is caused by the strong interaction of the localized electromagnetic field at ENZ layer with adjacent MO BIG:YIG layer. Note also the localization of H_y at the dielectric/metal interface in (b), thus showing the excitation of SPP mode. *Figure taken from PRB* ***96****, 075415 (2017).*

The TMOKE amplitude is again noted to be preferentially positive/negative in the quasi-matching of PA ENZ and SPP modes, while an oscillatory behavior should be observed in the matching condition. This actually further confirms that the ENZ-SPP coupling is responsible for the enhanced TMOKE. The effective medium approximation was made by considering that the thickness of each layer satisfies the subwavelength condition[74] $d_{\mathrm{SiO_2}}, d_{\mathrm{MO}}, d_{\mathrm{ITO}} \lesssim \lambda_0/10$, where $d_{\mathrm{SiO_2}}, d_{\mathrm{MO}}, d_{\mathrm{ITO}}$ are the thicknesses of the SiO_2, BIG:YIG, and ITO layers. Thus, we have used[75–79]

$$\varepsilon_{\parallel} = f_{\mathrm{ITO}}\varepsilon_{\mathrm{ITO}} + f_{\mathrm{MO}}\varepsilon_{\mathrm{MO}} + f_{\mathrm{SiO_2}}\varepsilon_{\mathrm{SiO_2}}, \quad (3.34)$$

$$\varepsilon_{\perp} = \frac{\varepsilon_{\mathrm{ITO}}\varepsilon_{\mathrm{MO}}\varepsilon_{\mathrm{SiO_2}}}{f_{\mathrm{SiO_2}}\varepsilon_{\mathrm{ITO}}\varepsilon_{\mathrm{MO}} + f_{\mathrm{MO}}\varepsilon_{\mathrm{ITO}}\varepsilon_{\mathrm{SiO_2}} + f_{\mathrm{ITO}}\varepsilon_{\mathrm{MO}}\varepsilon_{\mathrm{SiO_2}}}, \quad (3.35)$$

$$\varepsilon_{xz} = f_{\mathrm{MO}}\varepsilon_{xz,\mathrm{MO}}, \quad (3.36)$$

in Eqs. (3.30)-(3.33), where subindices ITO, MO, and SiO_2 denote the parameters corresponding to ITO, BIG-YIG, and SiO_2 materials, respectively. The filling ratios of SiO_2, BIG-YIG and ITO can be defined as $f_{\mathrm{SiO_2}} = \frac{d_{\mathrm{SiO_2}}}{d}$, $f_{\mathrm{MO}} = \frac{d_{\mathrm{MO}}}{d}$ and $f_{\mathrm{ITO}} = 1.0 - f_{\mathrm{SiO_2}} - f_{\mathrm{MO}}$, with d being the total thickness of the structure, $d = d_{\mathrm{ITO}} + d_{\mathrm{SiO_2}} + d_{\mathrm{MO}}$.

The mechanism responsible for the high sensitivity in the architecture in Fig. 3.10(a) can be further supported by the corresponding magnitudes for the electric and magnetic field profiles, $|E_z|$ and $|H_y|$, along the structure. Fig. 3.11(a) shows a localized electric field strongly enhanced in the ITO film, thus leading to enhanced MO interactions with the adjacent BIG-YIG layer. Strongly enhanced MO phenomena are produced while the magnetic field is enhanced at the dielectric/metal interface, as seen in Fig. 3.11(b), thus corroborating the excitation of a SPP resonance.

In summary, we have shown that the resonant tunneling and the coupling of perfectly absorbing ENZ modes with SPP resonances in magneto-photonic structures enhances TMOKE up to giant values. In some cases, TMOKE could reach the maximum theoretical amplitudes of ± 1, to be compared with the typical 10^{-3} in conventional ferromagnetic materials. The concepts introduced open up the possibility for the design and development of highly integrated nanometer-sized magneto-plasmonic devices. By way of illustration, we described the case of a realistic multilayer architecture that can be used as sensing/biosensing platform with proper functionalization.

Chapter 4

Repulsion of polarized particles near magneto-optical metamaterial

Contents

The levitation of objects with action at a distance has always been intriguing to humans. A fascinating approach for levitation involving electromagnetic fields was proposed by Francisco J. Rodriguez-Fortuño *et al.* [37]: they showed that a special subcategory of metamaterials, called epsilon-near-zero (ENZ) materials, can exhibit an electric classic analogue to Meissner effect[1], exerting repulsion on nearby sources. They concluded that this was possible because in an ENZ substrate, the normal component of the electric displacement **D** by a polarized particle will be expelled in analogous (but classic) fashion to the Meissner effect, and thus can result in levitation of the particle. This is because the normal component of **D** is conserved at the interface, as in for any finite-conductivity dielectric, but at the boundary of ENZ material is null, creating a gradient of electric field which could finally be understood as the existence of an electromagnetic force over the polarized particle. Later, they generalized the concept to include anisotropic metamaterials[38] with an effective permittivity tensor given by $\varepsilon_{eff} = diag(\varepsilon_{\parallel}, \varepsilon_{\parallel}, \varepsilon_{\perp})$, showing that an induced electric dipole placed near to an anisotropic substrate can experiment a repulsive force, if one of the diagonal components of permittivity tensor is close to zero. This can be checked in the repulsion condition in the quasistatic approximation

$$\mid \varepsilon_{\parallel} \mid\mid \varepsilon_{\perp} \mid < 1. \tag{4.1}$$

In particular, if one of the components of the permittivity tensor tends to zero, $\mid \varepsilon_{\parallel} \mid \approx 0$ or $\mid \varepsilon_{\perp} \mid \approx 0$, the value of their respective counterpart components can be high without affecting the repulsion condition. Here, we analyse for first time the contribution of the Magneto-Optic in the repulsive force of dipole particles. Specifically,

[1]The magnetic field created by a permanent magnet cannot penetrate into a superconductor substrate, leading to a levitation of the magnet.

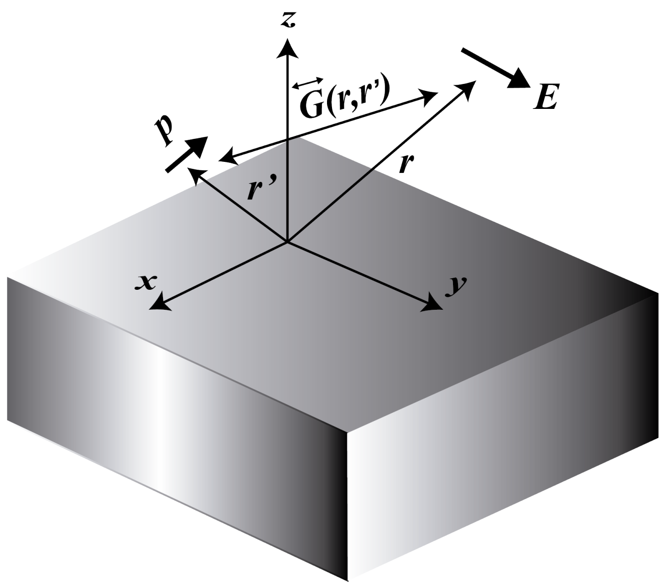

Figure 4.1: Illustration of the dyadic Green's function $G(r, r')$. The Green's function renders the electric field at the point **r** due to an electric dipole at point **r'**.

we have shown[80] that a particle emitting close to a MO metamaterial substrate can experiment a repulsive force if the magnetization is placed along the surface plane. We also derived the analytical condition for the existence of such repulsive force within the near-field approximation. Significantly, the repulsive force can be tuned by varying the filling fraction in a stack of two alternating layers of a metallic magneto-optical material and a dielectric. Potential applications can be envisaged for nanomechanical devices, particularly since similar metamaterial architectures have already been developed experimentally.

4.1 Dipole emission near planar MO interface

The problem of dipole radiation near to planar layered media is important to many fields of study. It is encountered in antenna theory, single molecule spectroscopy, cavity quantum electrodynamics, integrated optics, circuit design (microstrips), and surface contamination control. The relevant theory was also applied to explain the strongly enhanced Raman effect of adsorbed molecules on noble metal surfaces, and in surface science and electrochemistry for the study of optical properties of molecular systems adsorbed on solid surfaces. Detailed literature on the latter topic is given in Ref. [54]. In the context of near-field optics, dipoles close to a planar interface have been considered by various authors to simulate tiny light sources and small scattering particles [82]. In Fig. 4.1., we have an electric dipole located at the source point r'. The electric field created by this particle over a substrate can be obtained by using the concept of the dyadic Green's function:

$$E(r) = \omega^2 \mu_0 \mu G(r, r')\mathbf{p}, \tag{4.2}$$

which we shall use to calculate the force exerted over an electric point dipole source, emitting at a distance h, above a transversally magnetized MO metamaterial. Two possible configurations exist, as shown in Fig. 4.2, with the electric dipole moment oriented either vertically (VED) or horizontally (HED). In the horizontal configuration, the dipole may be parallel or normal to the magnetization $\mathbf{M}$. The surface along the xy-plane will be considered infinite. The corresponding dipole moment is considered as $\mathbf{p}$, oscillating with a frequency ω, embedded in a medium with isotropic permittivity ε_1.

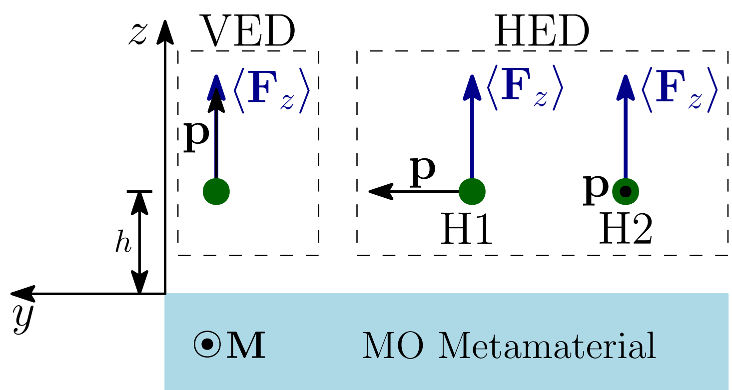

Figure 4.2: Pictorial view of the three possible orientations of the oscillating electric dipole, emitting at a distance h above a magneto-optical (MO) metamaterial. VED, H1 and H2 denote the vertical and the two possible horizontal configurations, respectively. $\mathbf{M}$ and $\mathbf{p}$ depict the magnetization of the surface and the electric dipolar moment, respectively. *Figure taken from PRB **94**, 245230 (2016).*

The complete force acting on the dipole source can be computed as[43]

$$\mathbf{F}(t) = (\mathbf{p} \cdot \nabla)\, \mathbf{E}_0 + \frac{\partial \mathbf{p}}{\partial t} \times \mathbf{B} + \frac{\partial \mathbf{r}}{\partial t} \times (\mathbf{p} \cdot \nabla)\, \mathbf{B}, \tag{4.3}$$

where $\mathbf{B} = \mathbf{B}_0 + \mathbf{B}_M$, with $\mathbf{B}_0$ and $\mathbf{B}_M$ being the magnetic inductions due to the reflected field and the stationary magnetization of the surface, respectively. In the horizontal configuration H2, the magnetization does not contribute to the Lorentz force since $\mathbf{p} \parallel \mathbf{M}$. For the other two configurations a contribution from $\mathbf{B}_M$ would be expected, but for the optical frequencies involved in many experiments only the time average of the electromagnetic force is observed. Thus, if we consider a harmonic time-dependence for all fields, i.e., $\mathbf{E}_0 \sim e^{-i\omega t}$, $\mathbf{B}_0 \sim e^{-i\omega t}$, and $\mathbf{p} \sim e^{-i\omega t}$, and take the time-average of Eq. (4.3), we obtain

$$\langle F_i \rangle = \frac{1}{2}\Re\left\{\mathbf{p}^* \cdot \partial_i \mathbf{E}\right\}, \tag{4.4}$$

with $i = x, y, z$. Lateral forces can appear on dipoles with general polarizations, such as circular,[44–46] but here we shall focus only on the vertical force, along the z-axis, expelling the particle from the MO surface,

$$\langle F_z \rangle = \frac{1}{2}\Re\left\{p_x^* \partial_z E_{x0} + p_y^* \partial_z E_{y0} + p_z^* \partial_z E_{z0}\right\}. \tag{4.5}$$

As the dipole source "feels" the MO metamaterial through the reflected fields, and therefore information about the substrate is entirely contained in the Fresnel coefficients, r_s and r_p, for s- and p-polarizations, we need to know the components of reflected electric field to compute this force. To obtain this reflected field one needs to use the concept of the dyadic Green's function Eq. 4.2, which gives the electric field $\mathbf{E} = \mathbf{G}\left(\mathbf{r}, \mathbf{r'}\right)\mathbf{p}$ at point $\mathbf{r}$ generated by a radiating electric dipole $\mathbf{p}$ located at point $\mathbf{r'}$. The Green's function of the reflected fields that interact at the dipole's origin ($\mathbf{r}_0 = h\hat{\mathbf{z}}$) is defined as

$$\mathbf{G}\left(\mathbf{r}_0, \mathbf{r}_0\right) = \frac{i}{8\pi\varepsilon_1}\int_0^\infty \frac{\kappa_\rho}{\kappa_{z1}} \begin{bmatrix} \kappa_1^2 r^s - \kappa_{z1}^2 r^p & 0 & 0 \\ 0 & \kappa_1^2 r^s - \kappa_{z1}^2 r^p & 0 \\ 0 & 0 & 2\kappa_\rho^2 r^p \end{bmatrix} e^{2i\kappa_{z1}h} d\kappa_\rho, \tag{4.6}$$

with $\kappa_1 = \frac{\omega}{c} n_1$ and $n_1 = \sqrt{\varepsilon_1}\sqrt{\mu_1}$ being the wave vector and refractive index of the upper medium, respectively, and $\kappa_{z1} = \kappa_1\sqrt{1 - \eta^2}$, with $\eta = \kappa_\rho/\kappa_1$. The transversal wave vector in cylindrical coordinates is denoted by κ_ρ. The derivative of Eq. (4.7) with respect to z can be easily obtained as:

$$\frac{\partial \mathbf{G}\left(\mathbf{r}_0, \mathbf{r}_0\right)}{\partial z} = \frac{-1}{8\pi\varepsilon_1}\int_0^\infty \kappa_\rho \begin{bmatrix} \kappa_1^2 r^s - \kappa_{z1}^2 r^p & 0 & 0 \\ 0 & \kappa_1^2 r^s - \kappa_{z1}^2 r^p & 0 \\ 0 & 0 & 2\kappa_\rho^2 r^p \end{bmatrix} e^{2i\kappa_{z1}h} d\kappa_\rho. \tag{4.7}$$

By separating the dipole moment, $\mathbf{p}$, into its transversal, $\left|p_\parallel\right|^2 = |p_x|^2 + |p_y|^2$, and longitudinal, $|p_\perp|^2 = |p_z|^2$, components, we can write

$$\frac{\partial \mathbf{G}\left(\mathbf{r}_0, \mathbf{r}_0\right)}{\partial z} = \frac{\partial \mathbf{G}_\parallel\left(\mathbf{r}_0, \mathbf{r}_0\right)}{\partial z} + \frac{\partial \mathbf{G}_\perp\left(\mathbf{r}_0, \mathbf{r}_0\right)}{\partial z}. \tag{4.8}$$

Hence, the time-averaged force over the z-axis can be written as[37]

$$\begin{aligned} \langle F_z \rangle = &\frac{1}{2}\Re\Bigg\{-\frac{1}{8\pi\varepsilon_1}\int_0^\infty \kappa_\rho\Big[\left|p_\parallel\right|^2\left(\kappa_1^2 r_s - \kappa_{z1}^2 r_p\right) \\ &+ 2\kappa_\rho^2 r_p \left|p_\perp\right|^2\Big] e^{i2h\kappa_{z1}} d\kappa_\rho\Bigg\}, \end{aligned} \tag{4.9}$$

where we have taken into account that the force is the same for H1 and H2 configurations, and therefore we shall not distinguish them, which will be referred to as HED configuration.

For calculation purposes, we considered the magnetization of the MO metamaterial as being along the x-axis (see transversal configuration in Fig. 1.2). Then, the corresponding permittivity tensor can be written as

$$\varepsilon = \begin{pmatrix} \varepsilon_{xx} & 0 & 0 \\ 0 & \varepsilon_{yy} & \varepsilon_{yz} \\ 0 & \varepsilon_{zy} & \varepsilon_{zz} \end{pmatrix} \tag{4.10}$$

where $\varepsilon_{xx} = \varepsilon_{yy} = \varepsilon_{\parallel} = \varepsilon^r_{\parallel} + \varepsilon^i_{\parallel}$, $\varepsilon_{zz} = \varepsilon_{\perp} = \varepsilon^r_{\perp} + i\varepsilon^i_{\perp}$, and $\varepsilon_{zy} = -\varepsilon_{yz} = \varepsilon^r_{zy} + i\varepsilon^i_{zy}$, with superindices r and i denoting the real and imaginary parts, respectively, while subindices $\parallel$ and $\perp$ denote the ε components parallel and orthogonal to the xy-plane. The Fresnel coefficients, used in Eq. (4.9), were analytically obtained as

$$r_p = \frac{-\frac{\varepsilon_1\eta^2}{\sqrt{1-\eta^2}} - \eta\varepsilon_{zy} - \varepsilon_{\perp}\sqrt{\varepsilon_{\parallel} + \frac{\varepsilon_{zy}^2 - \varepsilon_1\eta^2\varepsilon_{\parallel}}{\varepsilon_{\perp}}} + \varepsilon_{\perp}}{\frac{\varepsilon_1\eta^2}{\sqrt{1-\eta^2}} + \eta\varepsilon_{zy} - \varepsilon_{\perp}\sqrt{\varepsilon_{\parallel} + \frac{\varepsilon_{zy}^2 - \varepsilon_1\eta^2\varepsilon_{\parallel}}{\varepsilon_{\perp}}} - \varepsilon_{\perp}}, \tag{4.11}$$

$$r_s = \frac{-\sqrt{\varepsilon_1 - \eta^2} + \sqrt{\varepsilon_{\parallel} - \varepsilon_1\eta^2}}{\sqrt{\varepsilon_1 - \eta^2} + \sqrt{\varepsilon_{\parallel} - \varepsilon_1\eta^2}}. \tag{4.12}$$

Within the NF approximation, i.e., the height to wavelength ratio being $h/\lambda \ll 1$, we have $\kappa_1 \ll \kappa_\rho$. Since $\eta = \frac{\kappa_\rho}{\kappa_1}$ then $\eta \to \infty$. This approximation enables to simplify the Fresnel reflection coefficients

$$r_{p,\mathrm{NF}} = \lim_{\eta\to\infty} r^p = \frac{\sqrt{\varepsilon_{\parallel}\varepsilon_{\perp}} - i\varepsilon_{zy} - \varepsilon_1}{\sqrt{\varepsilon_{\parallel}\varepsilon_{\perp}} + i\varepsilon_{zy} + \varepsilon_1}, \tag{4.13}$$

and

$$r_{s,\mathrm{NF}} = \lim_{\eta\to\infty} r^s = 0, \tag{4.14}$$

which can be used to obtain the time-averaged force per unit radiated power[37] as

$$\frac{\langle F_z\rangle_{\mathrm{NF}}}{P_{\mathrm{rad}}} = -\sigma\frac{9n_1}{512\pi^4 c}\Re\left\{\frac{\sqrt{\varepsilon_{\parallel}\varepsilon_{\perp}} - i\varepsilon_{zy} - \varepsilon_1}{\sqrt{\varepsilon_{\parallel}\varepsilon_{\perp}} - i\varepsilon_{zy} + \varepsilon_1}\right\}\left(\frac{h}{\lambda}\right)^{-4}, \tag{4.15}$$

with $\sigma = 1$ and 2 for HED and VED configurations, respectively, where c is the speed of light in vacuum, and $P_{\mathrm{rad}} = \frac{\omega^4|\mathbf{p}|^2}{12\pi c^3}n_1$ is the radiated power of an electric dipolar source. We took the magnetic permeability $\mu = 1$ for all the media considered, thus the Fresnel coefficient for s-polarized waves is null in the NF regime.

The force acting on the oscillating electric point dipole is repulsive (attractive) if Eq. (4.15) is positive (negative). Thus, the sufficient condition to ensure the existence of a repulsive force in the NF approximation is $\Re\{r_{p,\mathrm{NF}}\} < 0$.[38] Upon separating Eq. (4.13) into its real and imaginary parts, one may determine the condition for repulsion of the dipole by the MO metamaterial analytically as

$$\left|\varepsilon_{\|}\right| \left|\varepsilon_{\perp}\right| < \varepsilon_1 \left(\varepsilon_1 + 2\varepsilon_{zy}^i\right) + \left|\varepsilon_{zy}\right|^2 , \tag{4.16}$$

where $|\varepsilon|^2 = \varepsilon^\dagger \varepsilon$, with † denoting the complex conjugate. If $\varepsilon_{zy} = 0$ this condition reduces to the one in Ref. [38] for uniaxial anisotropic metamaterials, which should work for ε-near-zero metamaterials at $\varepsilon_1 = 1$. The result in Eq. (4.16) indicates that the repulsive force condition can be tuned through ε_{zy} values, which can be tailored with an appropriate design of a microstructured MO metamaterial.[41,42] The condition for reaching a repulsive force is therefore much less strict than the previous ones for isotropic[37] and anisotropic[38] substrates.

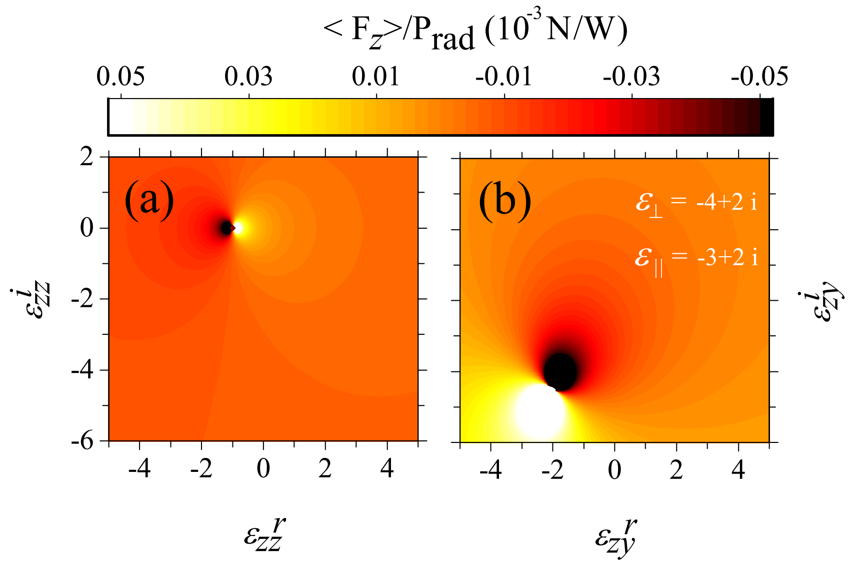

Figure 4.3: The time-averaged vertical force per unit radiated power, $\langle F_z \rangle / P_{\mathrm{rad}}$, for a VED near (a) an isotropic surface and (b) a hypothetical anisotropic MO metamaterial surface. Results were obtained for $h/\lambda = 0.1$. *Figure taken from PRB **94**, 245230 (2016).*

In Fig. 4.3 we show the vertical force, calculated from Eq. (4.9), acting on the VED configuration with $h/\lambda = 0.1$. The numerical results were obtained for an oscillating electric dipole near the surface between two semi-infinite media. For the sake of comparison we considered two cases. The first one, in Fig. 4.3(a), consists of an oscillating electric dipole in air/vacuum near an isotropic surface, while for the second one, in Fig. 4.3(b), the dipole oscillates near an anisotropic MO metamaterial surface. In the latter case, hypothetical values for $\varepsilon_{\parallel}$ and $\varepsilon_{\perp}$ were used to study the behavior of the force as a function of ε_{zy} components. Fig. 4.3(a) shows that for a metallic surface, repulsion can only be reached in the region ε-near-zero, as demonstrated in Ref. [37]. In contrast, for an anisotropic metamaterial MO surface, repulsion can occur even far from the ε-near-zero condition, as shown in Fig. 4.3(b). It is worth noting that these results are very robust to losses, which does not apply to approaches based on ε-near-zero metamaterials.[37,38]

There are several concepts for the design and development of MO metamaterials.[41,42] Here we consider planar structures proposed in Ref. [42], for which a highly enhanced MO effect was observed at optical frequencies, in contrast to the extremely low values in natural materials. Our structure is a periodic multilayered system made by stacking alternating metallic-MO and dielectric slabs. The layer thicknesses are on the order of some few nanometers, $d \ll \lambda$, so that the multilayered system can be treated as an effective medium for optical waves. The MO and dielectric filling ratios can be defined as $f_{\rm MO} = \frac{d_{\rm MO}}{d}$ and $f_{\rm D} = 1.0 - f_{\rm MO}$, respectively. Since the off-diagonal terms in Eq. (4.10) are responsible for the MO effects, the idea behind these MO metamaterials is to obtain off-diagonal contributions comparable to the diagonal ones, which can be reached by tuning the filling ratio of the MO material in the unit cell.[42] The effective permittivity tensor components are determined, within the effective medium (EM) theory as[42,75–79,83]

$$\begin{aligned} \varepsilon_{\parallel} &= 1 + f_{\rm D}\chi_{\rm D} + f_{\rm MO}\chi_{\rm MO}, && (4.17)\\ \varepsilon_{\perp} &= \left(\frac{f_{\rm D}}{1+\chi_{\rm D}} + \frac{f_{\rm MO}}{1+\chi_{\rm MO}}\right)^{-1}, && (4.18)\\ \varepsilon_{zy} &= i f_{\rm MO}\chi_0, && (4.19) \end{aligned}$$

where χ denotes the corresponding susceptibility of the constituent materials, with subindices D and MO indicating the dielectric and MO materials, respectively.

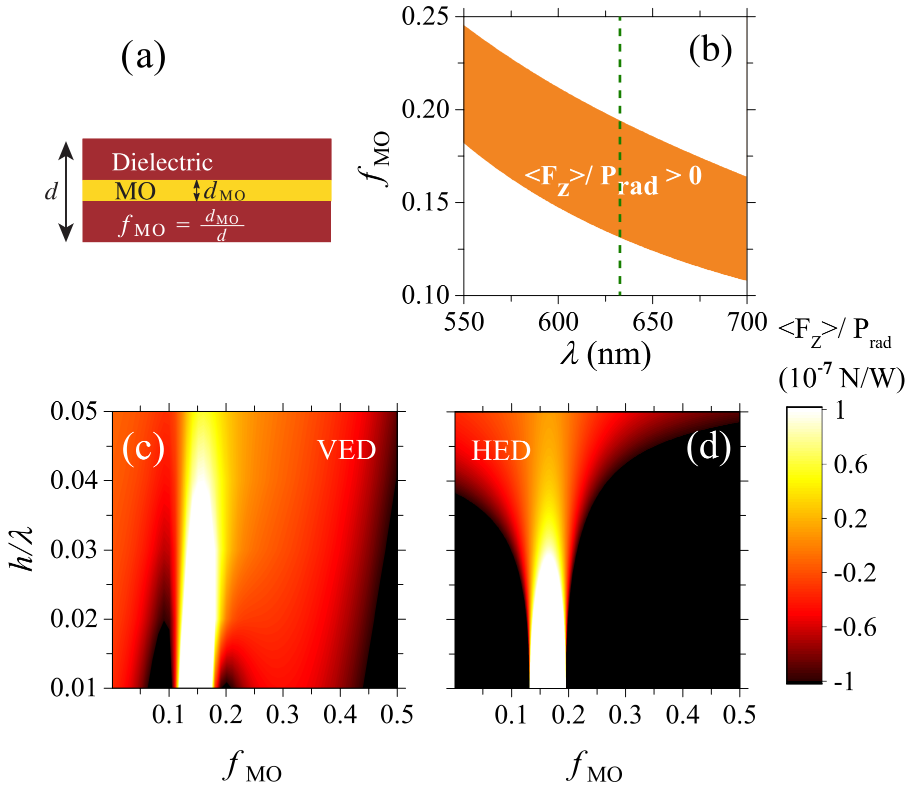

Figure 4.4: The time-averaged force acting on a (b)-(c) VED and a (d) HED source per unit radiated power as a function of the height over the substrate (vertical axis) and the filling ratio, f_{MO}, of the MO material in the unit cell, as depicted in (a). Dielectric layers were considered as made of SiO_2, while MO layers were taken as made of Co_6Ag_{94}. The vertical dashed line in (b) marks the results for $\lambda = 631$ nm. *Figure taken from PRB **94**, 245230 (2016).*

In order to work with an experimentally realizable MO metamaterial, in Fig. 4.4(a) we depict the geometry of a unit cell where the metallic-MO[53] and dielectric[54] materials are Co_6Ag_{94} and SiO_2, respectively. The time averaged force per unit radiated power calculated from Eq. (4.15), within the NF approximation, is plotted in Fig. 4.4(b) for a VED in air/vacuum, $z > 0$, radiating near an effective semi-infinite MO metamaterial located in the region $z < 0$. The results are presented as function of f_{MO} and the dipole radiation wavelength λ, with $h/\lambda = 0.01$. The region for repulsion varies with f_{MO} and λ, but retaining almost the same thickness. This can be understood in terms of the susceptibility χ_{MO} of the Co_6Ag_{94} material as function of λ and the increasing of h in order to fulfill the requirement $h/\lambda = 0.01$. In Figs. 4.4(c)-(d) we show the time averaged force per unit radiated power, from Eq. (4.9), as function of h and f_{MO} for a

VED and a HED, in air/vacuum, emitting just above a MO metamaterial superlattice composed by six unit cells. The unit cell thickness was taken as $d = 10$ nm, with $h/\lambda = 0.01$, and $\chi_{\mathrm{MO}} = -11.51 + 2.1i$, $\chi_0 = 2.1 - 1.15i$, and $\chi_{\mathrm{D}} = 1.12$, corresponding to an optical working wavelength of $\lambda = 631$ nm. The repulsive region in Figures 3c and 3d, as a function of f_{MO}, is consistent with the region along the vertical dashed line in Fig. 4.4(b), obtained within the NF approximation.

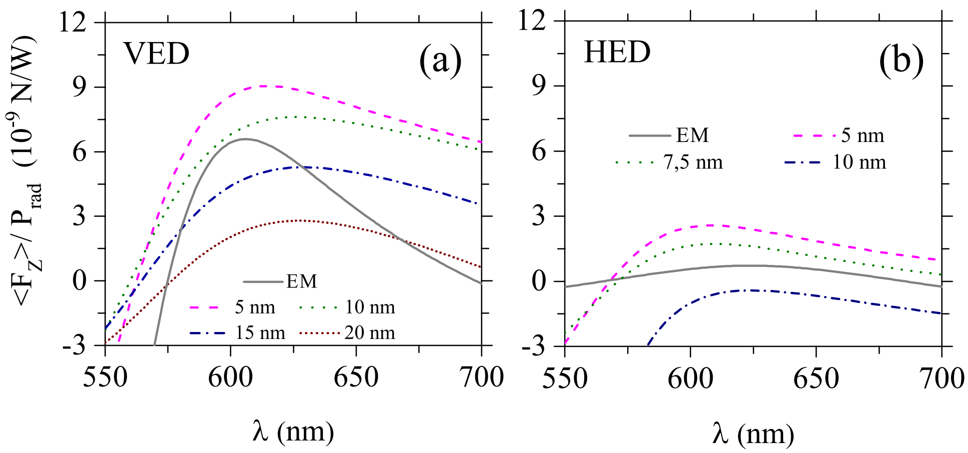

Figure 4.5: The time-averaged force per unit radiated power versus λ for (a) VED and (b) HED configurations. The results within the EM approximation (solid lines) are compared with the ones for the finite metamaterial superlattices with different period lengths, d. The MO filling ratio was $f_{\mathrm{MO}} = 0.17$ in all cases. *Figure taken from PRB **94**, 245230 (2016).*

Figs. 4.5 and 4.6 show the time averaged force per unit radiated power for VED and HED configurations, obtained from Eq. (4.9), versus the dipole radiation wavelength, λ, and the vertical distance to the MO surface, h, respectively. The MO filling fraction was taken as $f_{\mathrm{MO}} = 0.17$ in both cases. Results from the EM approximation (solid lines) are compared with the ones for metamaterial superlattices, composed by six unit cells, with different period lengths, d. The repulsive force decreases with an increasing period length owing to the rapidly decaying near fields dominating the force, as explained in detail in Refs. [38] and [86].

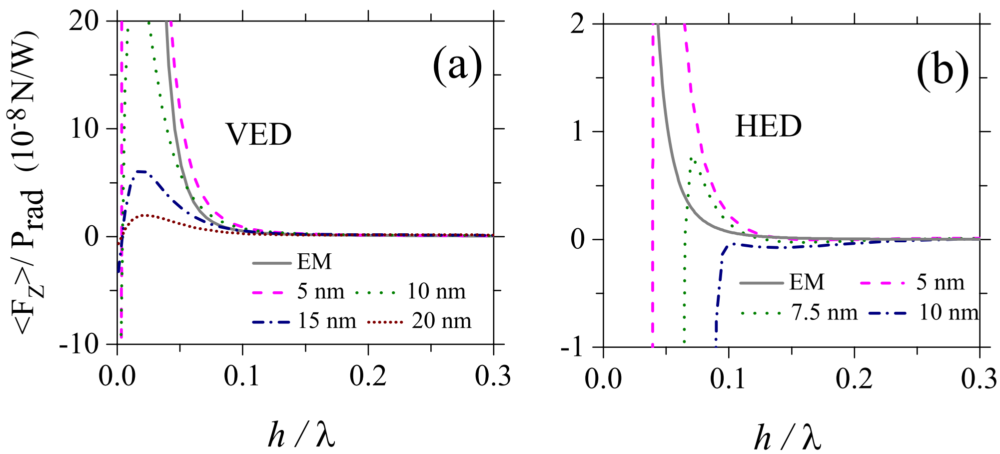

Figure 4.6: The time-averaged force per unit radiated power versus h for (a) VED and (b) HED configurations. The results within the EM approximation (solid lines) are compared with those for the finite metamaterial superlattices with different period lengths, d. The MO filling ratio and the optical working wavelength were taken as $f_{\mathrm{MO}} = 0.17$ and $\lambda = 631$ nm, respectively. *Figure taken from PRB **94**, 245230 (2016).*

As the calculation model used here works in scenarios which can be approximated by an electric dipole,[38] in Fig. 4.7 we use it to study the vertical time-averaged optical force acting over an illuminated nanoparticle near a MO metamaterial surface. In order to do that, we consider a Ag/SiO_2 core-shell nanoparticle[84] with inner and outer radii as $r_{\mathrm{in}} = 27.1$ nm and $r_{\mathrm{out}} = 30$ nm, designed to have a resonant polarizability near 650 nm. Thus, there are two forces acting on the nanoparticle: the first one, $\langle F_z\rangle_{\mathrm{pw}}$, arises from the standing plane wave illuminating source, pushing the nanoparticle along the direction of light propagation; the second one, $\langle F_z\rangle_{\mathrm{s}}$, due to reflected dipolar scattering pulls the nanoparticle away from the surface. As observed in the figure, the total force, $\langle F_z\rangle_{\mathrm{tot}} = \langle F_z\rangle_{\mathrm{s}}^r + \langle F_z\rangle_{\mathrm{pw}}$, is dominated by $\langle F_z\rangle_{\mathrm{s}}^r$ in the near-field region, while $\langle F_z\rangle_{\mathrm{pw}}$ predominates at larger distances, as expected according to discussions above. This result is of high relevance for optical light trapping of nanoparticles.[87–90] In particular, the optical light trapping of particles in nano-optical cavities has been demonstrated in theoretical[88] and experimental[90] papers. On the other hand, the resonant modes of defective metamaterial photonic superlattices and Fabry-Pérot cavities have been shown to be analogous.[74] Thus, the present results should be applied for example to consider a nanoparticle coupled to the resonant mode in a MO metamaterial defective photonic superlattice, analogous to calculations in Ref. [88]. In the latter work, a dielectric nanosphere was made to levitate inside a Fabry-Pérot cavity owing to optomechanical and Casimir interactions.

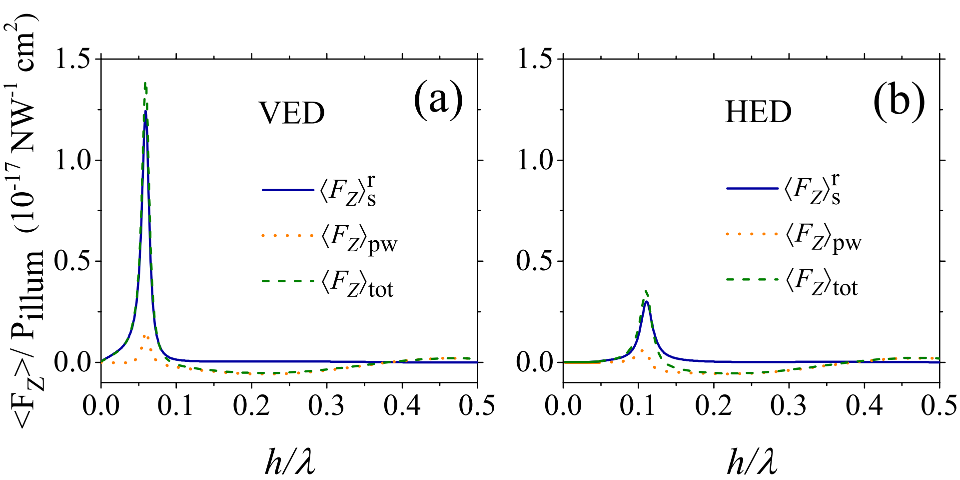

Figure 4.7: The time-averaged force per unit power of illumination versus h for a (a) VED and (b) HED configurations acting on a Ag/SiO$_2$ core-shell nanoparticle with radius $r = 57.1$ nm, close to a finite MO metamaterial superlattice, filling ratio $f_{\mathrm{MO}} = 0.15$ and unit cell thickness $d = 6$ nm. The illuminating wavelength was considered as $\lambda = 650$ nm, at normal incidence, with a power density of 1 Wcm^{-2} and nanoparticle polarizability[84] $(-3.92 + 2.37i) \times 10^{-32}$ CV^{-1}. *Figure taken from PRB **94**, 245230 (2016).*

In summary, we have shown for first time that the condition for levitation of electromagnetic sources near a substrates is greatly simplified if we allow the substrate to be magneto-optical. Upon designed a realistic MO metamaterial, we showed that a repulsive force can be generated regardless of material losses, whit a broad range of frequencies in the optical frequencies. We have obtained within the near-field approximation an analytical expression for the existence of such repulsive force, which can be tuned by varying the filling fraction of the MO metamaterial.

Chapter 5

Conclusions

We showed new properties of the magneto-photonic systems with applications in the design and development of sensing/biosensing platforms and nanomechanical structures, where the optical forces play an important role in the manipulation of small particles with light beams. First, we found new ways to enhance the transverse magneto-optical Kerr effect using MO metallic and epsilon-near-zero materials with realistic values, in very simple and compact systems. These extraordinary values were reached via the the excitation of resonant tunneling modes and the coupling of ε-near-zero with surface plasmon polariton modes, avoiding the use of prisms or gratings in sophisticated structures. Furthermore, we have shown the general relations to conveniently engineer the working wavelength by tuning the MO and dielectric material widths. On the other hand, we showed that repulsion of electromagnetic sources near a MO metamaterial can be reached in an enormously simplified way compared with their ε-near-zero counterparts. Upon designing a realistic MO metamaterial,[42] we showed that a repulsive force can be generated regardless of material losses, with broadband characteristic in the optical regime. Furthermore, in contrast to previous approaches, it can work in the dielectric regime far away from the ε-near-zero condition, making it suitable for realistic implementation.

Finally, we want to mention that our results have potential applications in thin-film optical devices for the design and development of future magneto-optical photonic circuits, biosensors and switches controlled by means of external applied magnetic fields. In the case of optical forces, we exemplified the repulsion of a dielectric nanoparticle, near a MO metamaterial surface, illuminated by a standing light source, which can be implemented for optical light trapping in MO metamaterial superlattices. Other examples may include radiating fluorescent particles, quantum dots or radiating microwave antennas.[38].

Chapter 6

Outlooks

Perspectives for future works are mainly focused in two directions. In the first one, we are interested into extend the calculations to consider second-order nonlinear effects. Thus, we expect to calculate the second-harmonic TMOKE by using reflected second-harmonic fields instead of linear reflectance values. Second, we will consider the magneto-optical effects in the calculation of lateral optical forces. The idea is to modify the lateral radiation pressure exerted by the light on a circularly polarized nanoparticle, which is emitting near a MO surface. These result would be of great importance for separation and/or manipulation of chiral molecules, which can have potential applications for medical and biological purposes.

Bibliography

[1] M. Faraday, Phil Trans. R. Soc. Lond. 1846, 136, 1.

[2] J. Kerr, Phil. Mag. 1877, 3, 321.

[3] A. Chizhik, A. Zhukov, J. M. Blanco, and J. Gonzalez, J. Magn. Magn. Mater. **249**, 27 (2002).

[4] A. A. Rzhevsky, B. B. Krichevtsov, D. E. Bürgler, and C. M. Schneider, Phys. Rev. B **75**, 144416 (2007).

[5] K. Kämpf, S. Kübler, F. W. Herberg, and A. Ehresmann, J. Appl. Phys. **112**, 034505 (2012).

[6] Y. Shoji, Y. Shirato, and T. Mizumoto, Jpn. J. Appl. Phys. **53**, 022202 (2014).

[7] A. V. Kimel, A. Kirilyuk, P. A. Usachev, R. V. Pisarev, A. M. Balbashov, and Th. Rasing, Nature **435**, 655 (2005).

[8] K. Vahaplar, A. M. Kalashnikova, A. V. Kimel, D. Hinzke, U. Nowak, R. Chantrell, A. Tsukamoto, A. Ithoh, A. Kirilyuk, and Th. Rasing, Phys. Rev. Lett. **103**, 117201 (2009).

[9] A. Kirilyuk, A. V. Kimel, and Th. Rasing, Rev. Mod. Phys. **82**, 2731 (2010).

[10] M. Pohl, L. E. Kreilkamp, V. I. Belotelov, I. A. Akimov, A. N. Kalish, N. E. Khokhlov, V. J. Yallapragada, A. V. Gopal, M. Nur-E-Alam, M. Vasiliev, D. R. Yakovlev, K. Alameh, A. K. Zvezdin, and M. Bayer, New J. Phys. **15**, 075024 (2013).

[11] V. I. Belotelov, D. A. Bykov, L. L. Doskolovich, A. N. Kalish, and A. K. Zvezdin, J. Opt. Soc. Am. B **26**, 1594 (2009).

[12] A. A. Grunin, A. G. Zhdanov, A. A. Ezhov, E. A. Ganshina, and A. A. Fedyanin, Appl. Phys. Lett. **97**, 261908 (2010).

[13] V. I. Belotelov, D. A. Bykov, L. L. Doskolovich, A. N. Kalish, and A. K. Zvezdin, J. Exp. Theor. Phys. **110**, 816 (2010).

[14] V. I. Belotelov, I. A. Akimov, M. Pohl, V. A. Kotov, S. Kasture, A. S. Vengurlekar, A. V. Gopal, D. R. Yakovlev, A. K. Zvezdin, and M. Bayer, Nature Nanotech. **6**, 370 (2011).

[15] L. E. Kreilkamp, V. I. Belotelov, J. Y. Chin, S. Neutzner, D. Dregely, T. Wehlus, I. A. Akimov, M. Bayer, B. Stritzker, and H. Giessen, “Waveguide-Plasmon Polaritons Enhance Transverse Magneto-Optical Kerr Effect," Phys. Rev. X **3**, 041019 (2013).

[16] M. Moccia, G. Castaldi, V. Galdi, A. Alù, and N. Engheta, J. Phys. D: Appl. Phys. **47** 025002 (2014).

[17] M. Moccia, G. Castaldi, V. Galdi, A. Alù, and N. Engheta, J. Appl. Phys. **115**, 043107 (2014).

[18] H. J. Williams, R. C. Sherwood, F. G. Foster, and E. M. Kelley, J. Appl. Phys. 28(10), 1181-1184 (1957).

[19] R. J. Gambino and T. Suzuki, IEEE, (2000).

[20] A. K. Zvezden and V. A. Kotov, *Modern Magnetooptics and Magnetooptical Materials*, 1st ed. (Taylor and Francis, London, 1997).

[21] G. Armelles, A. Cebollada, A. García-Martín, and M.U. González, Adv. Opt. Mater. 1, 10 (2013).

[22] M. Inoue, M. Levy and A. Baryshev, *Magnetophotonics: From Theory to Applications,* (Springer Series in Materials Sciences Vol. 178 (Springer-Verlag, Berlin Heidelberg, 2013), Chap. 4.

[23] D. Traviss, R. Bruck, B. Mills, M. Abb, and O. L. Muskens, Appl. Phys. Lett. **102**, 121112 (2013).

[24] S. Feng and K. Halterman, Phys. Rev. B **86** 165103 (2012).

[25] J. Yoon, M. Zhou, Md. A. Bashda, T. Y. Kim, Y. C. Jun, and C. K. Hwangbo, Scient. Rep. **5**, 12788 (2015).

[26] J. Park, J.-H. Kang, X. Liu, and M. L. Brongersma, Scient. Rep. **5**, 15754 (2015).

[27] J. A. Girón-Sedas, J. R. Mejía-Salazar, E. Moncada-Villa and N. Porras-Montenegro, Applied Phys. Lett **109**, 033106 (2016).

[28] J. A. Girón-Sedas, F. Reyes Gómez, Pablo Albella, J. R. Mejía-Salazar and Osvaldo N. Oliveira Jr., Phys. Rev. B **96**, 075415 (2017).

[29] R. Maboudian, R. T. Howe, J. Vac. Sci. Technol. B **15**, 1 (1997).

[30] N. Tas, T. Sonnenberg, H. Jansen, R. Legtenberg, M. Elwenspoek, J. Micromech. Microeng. **6**, 385 (1996).

[31] E. Buks and M. L. Roukes, Phys. Rev. B **63**, 033402 (2001).

[32] A. Ashkin and J. M. Dziedzic, Appl. Phys. Lett. **19**, 283 (1971).

[33] A. Ashkin and J. M. Dziedzic, Appl. Phys. Lett. **28**, 333 (1976).

[34] F. S. S. Rosa, D. A. R. Dalvit, and P.W. Milonni, Phys. Rev. Lett. **100**, 183602 (2008).

[35] J. N. Munday, F. Capasso, and V. A. Parsegian, Nature **457**, 170 (2009).

[36] R. Zhao, J. Zhou, Th. Koschny, E. N. Economou, and C. M. Soukoulis, Phys. Rev. Lett. **103**, 103602 (2009).

[37] F. J. Rodriguez-Fortuño, A. Vakil, and N. Engheta, Phys. Rev. Lett. **112**, 033902 (2014).

[38] F. J. Rodriguez-Fortuño, and A. V. Zayats, Light: Sci. App. **5**, e16022 (2016).

[39] P. Moitra, Y. Yang, Z. Anderson, I. I. Kravchenko, D. P. Briggs, and Jason Valentine, Nature Phot. **7**, 791 (2013).

[40] R. Maas, J. Parsons, N. Engheta, and A. Polman, Nature Photonics **7**, 907 (2013).

[41] B. Toal, M. McMillen, A. Murphy, W. Hendren, R. Atkinson, and R. Pollard, Mat. Res. Exp. **1**, 015801 (2014).

[42] X. Luo, M. Zhou, J. Liu, T. Qiu, and Z. Yu, Appl. Phys. Lett. **108**, 131104 (2016).

[43] P. C. Chaumet and M. Nieto-Vesperinas, Opt. Lett. **25**, 1065 (2000).

[44] F. J. Rodriguez-Fortuño, N. Engheta, A. Martinez, and A. V. Zayats, Nat. Comm. **6**, 8799 (2015).

[45] S. Shukov, V. Kajorndejnukul, R. R. Naraghi, and A. Dogariu, Nat. Photonics **9**, 809 (2015).

[46] S. Scheel, S. Y. Buhmann, C. Clausen, and P. Schneeweiss, Phys. Rev. A **92**, 043819 (2015).

[47] P. Yeh, Surface Science **96**, 41 (1980).

[48] D. M. Whittaker and I. S. Culshaw, Phys. Rev. B **60**, 2610 (1999).

[49] B. Caballero, A. García-Martín, and J. C. Cuevas, Phys. Rev. B **85**, 245103 (2012).

[50] A. K. Zvezdin and V. A. Kotov, 1st edn, London: Taylor and Francis, 1997.

[51] F. Abelés, Ann. Phys. **5**, 596-640, (1950).

[52] Š. Višňovský, “Optics in Magnetic Multilayers and Nanostructures," Taylor & Francis Group, (2006).

[53] S.-Y. Wang, W.-M. Zheng, D.-L. Qian, R.-J. Zhang, Y.-X. Zheng, S.-M. Zhou, Y.-M. Yang, B.-Y. Li, and L.-Y. Chen, J. Appl. Phys **85**, 5121 (1999).

[54] I. H. Malitson, J. Opt. Soc. Am. B **55**, 1205 (1965).

[55] S. Vassant, A. Archambault, F. Marquier, F. Pardo, U. Gennser, A. Cavanna, J. L. Pelouard, and J. J. Greffet, Phys. Rev. Lett. **109**, 237401 (2012).

[56] X. Sun, D. H. Kim, and H. S. Kwok, "Thin-film structures for photovoltaics : symposium held December 2-5," MRS - Materials Research Society, p.p. 267, 1998.

[57] I. A. Petukhov, A. N. Shatokhin, F. N. Putilin, M. N. Rumyantseva, V. F. Kozlovskii, A. M. Gaskov, D. A. Zuev, A. A. Lotin, O. A. Novodvorsky, and A. D. Khramova, Inorganic Materials **48**, 1020 (2012).

[58] S. Kang, S. Cho, P. Song, Thin Solid Films **559**, 92 (2014).

[59] H. Wang, H. Zhao, H. Su, G. Hu, and J. Zhang, Appl. Phys. Exp. **9**, 092201 (2016).

[60] E. Feigenbaum, K. Diest, and H. A. Atwater, Nano Lett. **10**, 2111 (2010).

[61] S. Q. Li, P. Guo, L. Zhang, W. Zhou, T. W. Odom, T. Seideman, J. B. Ketterson, and R. P. H. Chang, ACS Nano **5**, 9161 (2011).

[62] J. B. González-Díaz, A. García-Martín, G. Armelles, J. M. García-Martín, C. Clavero, A. Cebollada, R. A. Lukaszew, J. R. Skuza, D. P. Kumah, and R. Clarke, Phys. Rev. B **76**, 153402 (2007).

[63] Y. C. Jun, J. Reno, T. Ribaudo, E. Shaner, J.-J. Greffet, S. Vassant, F. Marquier, M. Sinclair, and I. Brener, Nano Lett. **13**, 5391 (2013).

[64] A. Hiraki, E. Lugujjo, and J. W. Mayer, J. Appl. Phys. **43**, 3643 (1972).

[65] T. Wehlus, T. Körner, S. Nowy, J. Frischeisen, H. Karl, B. Stritzker, W. Brütting, Phys. Stat. Sol. (a) **208**, 264 (2011).

[66] A. R. Davoyan, A. M. Mahmoud and N. Engheta, Opt. Exp. **21**, 3279 (2013).

[67] T. Gardner, C. Frisbie, M. Wrighton, J. Am. Chem. Soc. **117**, 6927 (1995).

[68] S. Oh, Y. Yun, D. Kim, and S. Han, Langmuir **15**, 4690 (1999).

[69] S. K. VanderKam , E. S. Gawalt , J. Schwartz , and A. B. Bocarsly, Langmuir **15**, 6598 (1999).

[70] C. Yan , M. Zharnikov , A. Gölzhäuser, and M. Grunze, Langmuir **16**, 6208 (2000).

[71] P. M. Armistead and H. H. Thorp, Anal. Chem. **72**, 3764 (2000).

[72] I. Markovich, D. Mandler, J. Electroanal. Chem. **500**, 453 (2001).

[73] X. Yang, Y. Yuan, Z. Dai, F. Liu, and J. Huang, Sensors and Actuators B: Chemical **237**, 150 (2016).

[74] A. E. B. Costa, J. R. Mejía-Salazar, and S. B. Cavalcanti, J. Opt. Soc. Am. B **33**, 468 (2016).

[75] D. J. Bergman, Phys. Rep. **43**, 377 (1978).

[76] M. Born and E. Wolf, Principles of Optics (Pergamon, New York, 1980).

[77] P. A. Belov and Y. Hao, Phys. Rev. B **73**, 113110 (2006).

[78] V. M. Agranovich and V. E. Kravtsov, Solid State Commun. **55**, 85 (1985).

[79] P. B. Catrysse and S. Fan, Phys. Rev. Lett. **106**, 223902 (2011).

[80] J. A. Girón-Sedas, J. R. Mejía-Salazar, J. C. Granada, and Osvaldo N. Oliveira Jr., Phys. Rev. B **94**, 245230 (2016).

[81] H. Metiu, "Surface enhanced spectroscopy",in Progress in Surface Science, I. Prigogine and S. A. Rice, eds., vol. 17, 153-320, New York: Pergamon Press (1984).

[82] L. Novotny, J. Opt. Soc. Am. A **14**, 91-104 and 105-113 (1997)

[83] P. B. Catrysse and S. Fan, Adv. Mater. **25**, 194 (2013).

[84] C. F. Bohren, D. R. Huffman, “Absorption and scattering of light by small particles". New York: John Wiley & Sons, Inc.; 1983.

[85] A. S. Shalin, P. Ginzburg, P. A. Belov, Y. S. Kivshar, A. V. Zayats, Laser Photon Rev. **8**, 131 (2014).

[86] O. Kidwai, S. V. Zhukovsky, J. E. Sipe, Phys. Rev. A **85**, 053842 (2012).

[87] J. Gieseler, B. Deutsch, R. Quidant, and L. Novotny, Phys. Rev. Lett. **109**, 103603 (2012).

[88] W. Nie, Y. Lan, Y. Li, and S. Zhu, Phys. Rev. A **88**, 063849 (2013).

[89] L. P. Neukirch, E. von Haartman, J. M. Rosenholm, and A. N. Vamivakas, Nature Phot. **9**, 653 (2015).

[90] P. Mestres, J. Berthelot, S. S. Aćiminović, and R. Quidant, Light: Sci. App. **5**, e16092 (2016).